VELOCITY MAP IMAGING APPARATUS FOR STUDIES ON THE PHOTOCHEMISTRY OF WATER ICE

by

Pubudu Piyumie Wickramasinghe

A thesis submitted to the Department of Chemistry

In conformity with the requirements for

the degree of Master of Science

Queen's University

Kingston, Ontario, Canada

(February, 2011)

Abstract

This work describes the design and development of a velocity map imaging apparatus that will be used to study the laser initiated photochemistry of water ice and other condensed phases. Experiments on methanol ice photolysis using a different apparatus at Kyoto University are described to give an appreciation of the photochemistry and the experimental parameters.

Water deposited on a surface at temperatures below 140 K can form an amorphous solid. Amorphous solid water (ASW), which does not exhibit properties of a well-defined phase, is the most profuse phase of water found in astrophysical environments. Chemical characteristics of ASW - in particular its photochemistry - and the physical characteristics closely associated with the structure such as density and surface are reviewed. The correlations between the morphology and the growth conditions of ASW are also described.

Methanol is also known to be a component on the icy mantle on interstellar grains. The effects of irradiating amorphous solid methanol by UV photons are discussed. Experiments at Kyoto University have been performed to detect state-selectively nascent OH and CH_3 photofragments following photolysis at 157 nm. Information on the velocity distributions was obtained from time-of-flight measurements.

At Queen's University Velocity Map Imaging combined with resonance enhance multiphoton ionization (REMPI) will be used for quantum state-selective detection of the nascent photoproducts and their velocity distribution. To help automate the experiments "virtual instruments" have been created for the hardware components of the experiment using LabVIEW 8.6. The ion optics of the velocity map imaging spectrometer under construction at Queen's have been characterized using the SIMION 7.0 software package, and the anticipated experimental image of nascent photoproducts has been simulated by a Monte-Carlo-type algorithm.

Acknowledgements

Many people have contributed to the completion of this thesis. I would like to express my deep-felt thanks to Professor Hans-Peter Loock for his guidance and encouragement, and Dr. Jack Barnes for his assistance through this research project. I am grateful to my co-workers in the Velocity Map Imaging group: Dr. Wei Guo for the help with LabVIEW programming, Jeff Crouse and Stephen Walker for the useful discussions. I would like to thank my peers in the Loock Lab: Jessica Litman, John Saunders, Klaus Bescherer, Hanna Omrani, and Helen Wächter for their friendship and support. I am grateful to Professor Masahiro Kawasaki and his research group for hosting my visit in Kyoto University, Japan.

The Queen's University Writing Centre has been a wonderful source for feedback on my writing and I am also thankful to Claire Hooker for proof-reading this thesis. I greatly appreciate the assistance of Dr. Arunima Khanna, and Barbara Fretz of Queen's University, Learning Strategies. My special thanks go to Barbara Schlafer, Gamila Abdulla, Karen Knight, and Lisa Webb of the Ban Righ Center for the inspiration they provide, and the numerous ways they have assisted me.

My heart-felt gratitude goes to Eily Strotmann, for "adopting" me as her granddaughter, helping me every step of the way and for making Canada my home away from home. I am grateful to Nancy Binks and Yolande Webb, for helping me in my hour of need.

Finally, I would like to thank my family. I have benefitted greatly from the many sacrifices my parents, Swarnamalie and Sarath Wickramasinghe have made. I could not appreciate them enough for all the love they have given me. I am thankful to my sister Sathika Wickramasinghe-my twin soul, my grandmother for her kindness, Chatura Hewavitharana for being my strength, my extended family for their support through the years, and to Professor Ruchira Cumaranatunga for being a lifelong inspiration. Thank you.

To Amma and Thaththa

Table of Contents

List of Figures

List of Tables

Chapter 1
Introduction

The investigation of the physical and chemical properties of vapor-deposited ice has received much attention in the recent years, primarily due to important astrochemical[1-3] and atmospheric[4-6] implications. Water ice in the cold, dense regions of interstellar clouds is a medium for photochemical reactions when exposed to ultraviolet (UV) radiation.[7, 8] On earth, polar regions act as sinks for atmospheric pollutants and UV photolysis of these compounds produces photoproducts that impact the environment. For example, heterogeneous reactions between water ice and molecules such as HCl, $ClONO_2$, and N_2O_5 in the stratosphere play a central role in the occurrence of the Antarctic ozone hole.[4] Furthermore, simple molecules such as CH_3OH, NH_3, CO, H_2 found on interstellar ices are considered to be the building blocks of the solar system as their interaction with UV radiation gives rise to complex molecules in molecular clouds.[9,10] Therefore, studies of ice photochemistry in the interstellar medium, in the polar regions and in the laboratory are of great importance.

With the novel Velocity Map Imaging apparatus under development at Queen's University, photochemical reactions on amorphous or polycrystalline ice and their contaminants can be studied in a controlled lab environment. The photoproducts, which are formed after irradiation of the ice matrix with a UV laser pulse, are detected quantum state selectively using a second UV laser through the resonance-enhanced multiphoton

ionization (REMPI) technique. The nascent photoproducts are then detected by projection on a position sensitive detector and their velocity and angular distributions are recorded. This process is called velocity map imaging (VMI). Using energy and momentum conservation it is then possible to calculate the energy transferred to the ice matrix. By characterizing the structural changes that take place in the ice matrix through Fourier Transform Infrared (FT-IR) spectroscopy, it is possible to obtain even more detail on the reaction mechanisms between water ice molecules and the photoproducts. The determination of kinetic and internal energy distributions of the nascent desorbed species together with the spectroscopic signatures of the ice matrix and the stable trapped photoproducts is expected to provide the complete photochemical mechanism. Preliminary work in support of the development of this apparatus has been conducted through a collaborative study involving the author and the Kawasaki Group at Kyoto University using a similar machine, albeit without velocity map imaging capabilities. The experiments with the Kawasaki group illustrate the capabilities and limits of the state selective detection of photoproducts following methanol ice photolysis.

In chapter 2 of this thesis an overview of the vast literature on the photochemistry of amorphous solid water and polycrystalline ice with a special emphasis on experimental studies of photoinduced reactions is provided. The phases of water ice found in interstellar ices, the properties of vapor-deposited water ice, spectroscopic characteristics of the ice matrix, the correlation between growth conditions and structure, and effects of photolysis on the ice matrix are presented.

The VMI apparatus at Queen's University and in particular the ion optics and software components are presented in Chapter 3. The kinetic and angular distributions of desorbed photoproducts can be determined by the back projection of the raw image of photofragments. A back projection method based on a Monte-Carlo simulation is presented in this section. The ability to synchronize the operation of individual instruments in the VMI apparatus will be critical in conducting an automated experiment. In Chapter 4, the programming of the instrumental components using LabVIEW 8.6 is discussed. Experimental components which were modified or constructed during the course of this work are also briefly described.

The mechanisms and dynamics of the production of CH_3 and OH from the 157 nm photodissociation of amorphous solid methanol at 90 K serves as a guide as to the data that may be expected. Preliminary studies on the photolysis of methanol ice were conducted using a TOF-MS apparatus at Kyoto University. In the final chapter the state-selective detection of OH and CH_3 photoproducts from the 157 nm photolysis of methanol ice is discussed and their REMPI spectra analysed. A plausible reaction mechanism and the energetics of the reaction are presented.

References for Chapter 1

[1]G. B. Hansen, T. B. MsCord, J. Geophys. Res., **109**, E01012 (2004).

[2]B. A. Smith, L. Soderbolem, R. Beebe, J. Joyce, G. Briggs, A. Bunker, S. A. Collins, C. J. Hansen, T.V. Johnson, J. L. Mitchell, R. J. Terrile, M. Carr, A. F. Cook II, J. Cuzzi, J. B. Pollack, G. E. Danielson, A. Ingersoll, M. E. Davies, G. E. Hunt, H. Masursky, E. Shoemaker, D. Morrison, T. Owen, C. Sagan, J. Ververka, R. Strom and V. E. Suomi, Science, **212**, 163 (1981).

[3]F. L. Whipple, Astrophys. J., 11, 375 (1950).

[4]M. A. Tolbert, A. M. Middlebrook, J. Geophys. Res., **95**, 22423 (1990).

[5]T. G. Koch, S. F. Banham, J. R. Sodeau, A. B. Horn, M. R. S. McCoustra, and M. A. Chesters, J. Geophys. Res., **102**, 1513 (1997).

[6]A. B. Horn, T. Koch, M. A. Chesters, M. R. S. McCoustra, and J. R. Sodeau, J. Phys. Chem. **98**, 946 (1991).

[7]S. Andersson, A. Al-Halabi, G.-J. Kroes, and E. W. Dishoeck, J. Chem. Phys. **124**, 064715 (2006).

[8]L. J. Allamandola, M. P. Bernstein, S. A. Sanford, and R. L. Walker, Space Sci. Rev. **90**, 219 (1999).

[9]N. Watanabe, and A. Kouchi, Prog. Surf. Sci. **83**, 439 (2008).

[10]E.Herbst, Chem. Soc. Rev. **30**, 168 (2001).

Chapter 2

Literature Review

2.0 Introduction

Amorphous Solid Water (ASW) is a major constituent in interstellar clouds[1], comets[2], satellites of outer planets[3], and icy grain mantles[4]. Thus, it has important astronomical implications. Also, water ice in the cubic or amorphous phase has been reported as a major component of the surface of many satellites and planetary rings.[3] On earth, heterogeneous reactions, occurring on the surfaces of polar stratospheric cloud particles, are recognized to play a central role in the photochemical mechanism responsible for the occurrence of the Antarctic ozone hole.[1] The crystallization process of ASW is important in physical phenomena associated with ices such as sublimation, the outgassing of volatile molecules, and changes in the thermal conductivity.[2,3] These properties are controlled to a large extent by changes in the hydrogen bonded network of the water during heating.[2] By characterizing the structural changes that occur within water ice, it may be possible to understand the chemistry of cometary and interstellar ice and stratospheric ice particles. Hence, the study of water ice at low temperatures and the ability of water ice to trap gases have received much attention. Photochemistry of water ice plays an important role in interstellar grain chemistry. For this reason, primary and secondary photodissociation reactions taking place on water have received extensive attention because of their importance in atmospheric chemistry and astrophysics.[1-6] This

chapter concerns the chemical behavior and structure of the ice surface, in particular with regards to the spectroscopy and the photolysis of surface ice films. This will be followed by a discussion of the photochemistry of water ice and of constituents in ice.

2. 1 Structure and Formation of water ice

The equilibrium structure within which a material crystallizes under given conditions of temperature and pressure is determined by the interaction forces between its molecules. The properties of ice have been interpreted by their crystal structure, forces between their constituent molecules, and their energy levels. The crystal structure of ice is formed with water molecules linked to each other so that each proton of one molecule is directed towards a lone pair electron hybrid of a neighboring molecule. The oxygen atoms in ice are arranged so that they are at the centre of a tetrahedron, with each oxygen atom positioned 2.76 Å away from four other oxygen atoms.[3-5]

The structure of water-rich ice in astrophysical environments is usually not that of the familiar thermodynamically stable hexagonal crystalline polymorph (I_h) found almost exclusively on Earth. Rather, astrophysical water ice is often observed to be in an amorphous form.[2] Temperature is the main factor determining the crystallographic phase of ice grown from the gas phase at low pressures.[3,4]

Narten *et al*.[5] reported that there are two evidently distinctive forms of amorphous ice which differ in density as well as in the second nearest-neighbour oxygen-oxygen distribution. The low-density form was estimated to be 0.94 g/cm^3 at 77 K and the high-density (I_ah) 1.1 g/cm^3 at 10 K. The nearest-neighbour O-O separation was 2.76 Å in the low-density form. The high-density form had similar an X-ray diffraction pattern similar to low-density amorphous ice. However, it showed an additional peak at 3.3 Å. Narten *et al*.[5] suggested that the increase in density was a consequence of water molecules occupying the distance between the first and second nearest neighbour at the interstitial sites of the network. The additional peak was caused by such water molecules and was the first indication of the occurrence of structural polymorphs of water.[6] Low-density amorphous ice produced by water vapour deposition below 130 K was determined to be a highly porous open network with a surface area of 150 - 500 m^2/g. This form of ice also has a noteworthy concentration of surface OH groups as observed through the measurements of surface area, density of ice films and IR spectroscopy of water ice.[5-8]

Furthermore, Jenniskens and Blake[8] designed experiments to simulate interstellar ices by observing the structural changes of vapor-deposited on water ice in vacuum between temperatures of 15 to 188 K. They reported the existence of three amorphous forms and two crystalline forms of water ice. High-density amorphous water ice (I_ah) is found at 15 K, the low-density form (I_al) between 38 to 68 K, and the restrained amorphous form (I_ar) preceding cubic ice (I_c) at 131 K.[2] When amorphous ice films are further annealed, crystalline ice transfers to polycrystalline cubic ice (I_c) and hexagonal ice (I_h). The I_h

phase prevalent on earth can also be produced directly by condensation onto a substrate cooled to temperatures above 190 K.[3] Condensation below 190 K but above 135 K leads to I_c.[3] If warmed between 160 - 200 K I_c will transform irreversibly into I_h. This wide temperature range has been attributed to the dependence of the crystallization temperature on the size of cubic ice crystals. These observations imply that the crystallization process, which commences just above the glass-to-liquid transition temperature, is incomplete because fragments of the non-crystalline microphases co-exists with I_c up to 200 K.[8,9] Amorphous ice is the dominant form at temperatures below 130 K. This phase of ice converts to I_c at a rate that depends on the temperature as given in Figure 1. I_ar coexists with I_c from 148 K until 188 K. The existence of I_ar is responsible for the irregular gas retention and gas release from water rich ices at temperatures above 150 K.[8] Figure 1 illustrates the existence of amorphous and crystalline ices at different temperatures.

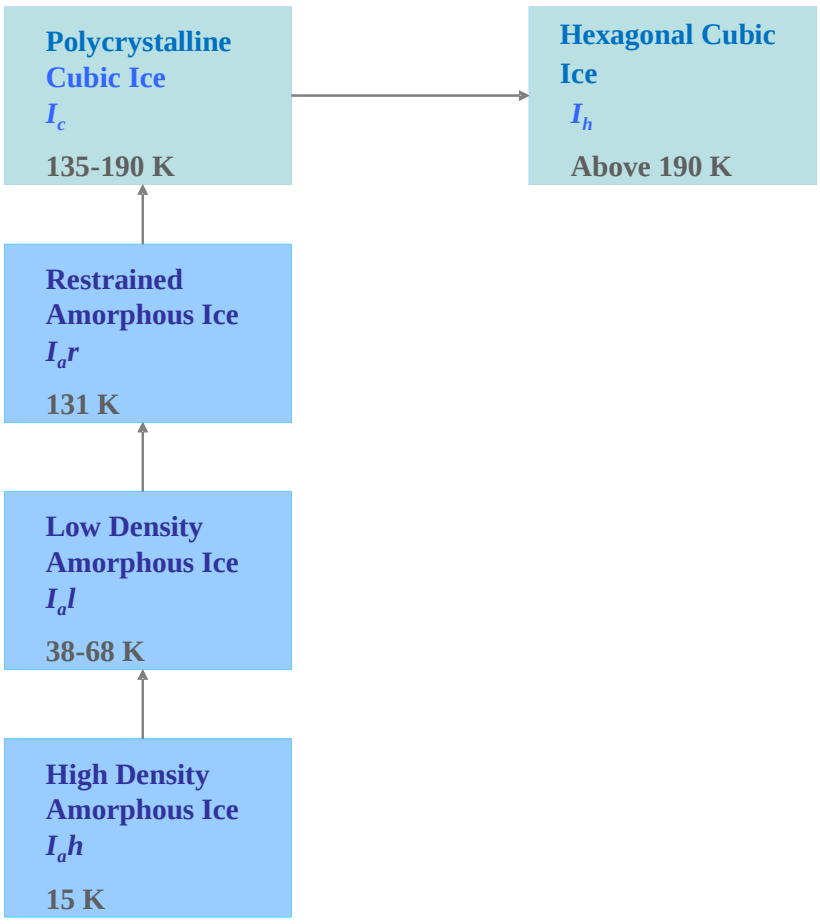

FIG.1. Structural dependence of ice on temperature.

In addition to this, Berland *et al.*[10] reported that the density of vapor-deposited ice films as a function of substrate temperature. At 35 K, the density of ice films was found to be 0.68 g/cm^3. This is considerably lower than 0.93 g/cm^3 for ice I_c. This low density is due to the formation of microporous amorphous ice. Furthermore, the density increased rapidly from 0.68 – 0.78 g/cm^3 for temperatures between 30 – 60 K, and from 0.80 – 0.93 g/cm^3 for temperatures between 80 K – 120 K. A density of 0.93 g/cm^3 was reported for ice films between temperatures 120 K - 150 K.

The structure of unannealed amorphous ice is found to have greater dispersion of O···O···O angles and nearest neighbor O-O separations and a larger mean separation than that of annealed amorphous and polycrystalline ice.[9] This gives rise to a more disordered structure in unannealed amorphous ice and results in a wider distribution of weaker hydrogen bond strengths. Of the solid forms of H_2O the unannealed amorphous ice is the most comparable structure to that of liquid water. The transition from I_ah to I_al is accountable for the diffusion and recombination of radicals of interstellar ices processed by ultraviolet radiation at low temperatures.[8]

2. 2 Spectroscopic studies of vapor-deposited ice films

2. 2. 1 Pure H_2O

The infrared spectra of all forms of solid water are characterized by four absorption bands. A sharp band is observed for the dangling OH-stretching mode from the ice surface at 3700 cm^{-1}. This intense band corresponds to the symmetric (υ_1) and antisymmetric (υ_3) modes in the isolated water molecule. A broad band is observed at 3370 cm^{-1} due to the OH-stretching mode in the bulk of amorphous ice at 98 K. The third band (1665 cm^{-1}, υ_2) is a result of the bending mode. The fourth prominent band observed at 763 cm^{-1} is a consequence of libration, i.e. the hindered rotation of the water molecule. In addition, comparatively weak combination bands are observed at 2205 cm^{-1} (3 υ_L or $\upsilon_2 + \upsilon_L$).[9-12] The IR absorption spectra of H_2O adsorbed on Au (111) are given in Figure 2.

The IR absorption features observed in the water molecule are dependent on the hydrogen bonding of the system. The difference between the vibration frequencies of H_2O molecules in the gas phase and the frequency in unannealed amorphous ice for the bending mode is +70 cm^{-1} and for the OH-stretching mode -450 cm^{-1}.[9] Elevated frequencies in libration and bending modes may be observed due to the presence of a strong hydrogen bonded network. Strong hydrogen bonds hinder libration and bending and weaken the normal OH-stretching frequencies.

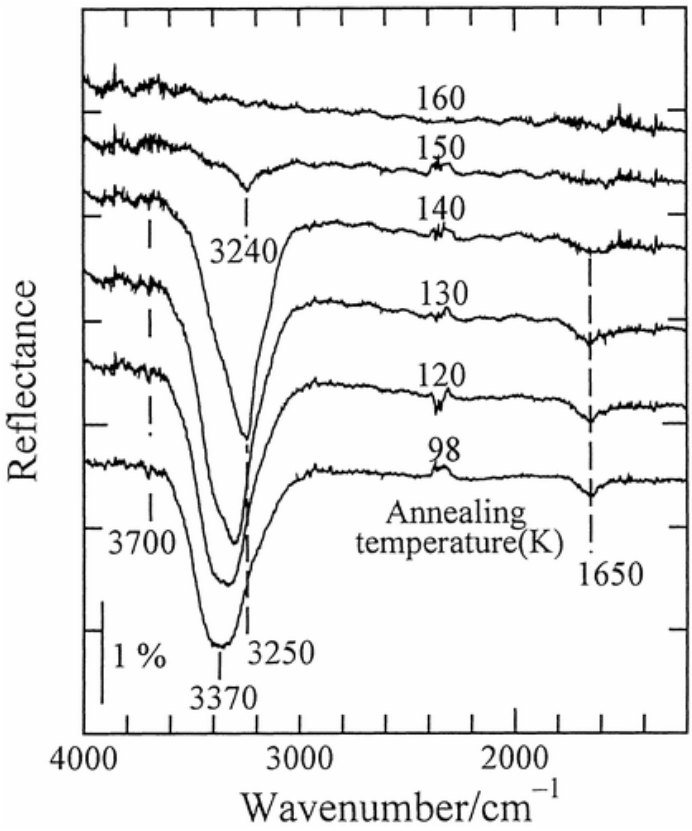

FIG.2. Temperature dependence of the IR absorption spectra of H_2O adsorbed on an Au (111) surface at 98 K. H_2O was first adsorbed at 98 K, and then the substrate was heated step wisely to the indicated temperature.

Reproduced from Sato *et al*.[12]

The effects of hydrogen bonding on the frequency and width of IR absorption features in amorphous ice was investigated by Hagen *et al.*[11] They reported that when amorphous ice is deposited at 10 K, and warmed up to 130 K, the bulk OH-stretching band shifted to 3250 cm^{-1}, the line width narrowed, the peak intensity increased and the libration frequency increased.[9] This was due to the increased strength in the hydrogen bond. Upon annealing to 130 K, amorphous ice deposited at 10 K undergoes an irreversible transformation to a more ordered form. With the annealing process, the distance between neighboring O-O positions decreases and the molecule reorients to optimize the preferably linear O-H···O bond angles. The smaller O-O separations result in strengthened hydrogen bonds. Jenniskens and Blake[8] reported that irreversible changes continue to occur in the same parameters when amorphous ice is kept at 140 K for a prolonged time.[8] These changes correspond to the transformation from amorphous ice to crystalline ice (I_c). Since these spectral changes start at temperatures as low as 120 K, it has been inferred that the phase change from amorphous ice to crystalline occurs above 120 K. The transformation is completed within 45 min.

2. 2. 2 Dangling OH

A fundamental characteristic of low-density amorphous ice is its microporosity. Amorphous ice formed below 90 K is a microporous network with a large surface area of approximately 400 m^2/g due to the presence of nanoscale pores. [13] Pore widths were measured to be less than 2 nm.[13]

The conventional four tetrahedral hydrogen bonds in water molecules are indicative of the condensed phase of H_2O. However, Rowland *et al.*[13] observed that water molecules on the pore surface cannot form these 4- coordinated/ tetrahedral hydrogen bonds. They reported that, as a consequence, dangling O-H groups that are weakly hydrogen bonded are formed on the pore surface. Vibrational spectroscopic studies of vapor-deposited ice films by Buch and Devlin[14] showed evidence of dangling O-H bonds for ice films deposited at low temperatures. The existence of these dangling O-H bonds designates vacancies in the ice network that are a distinctive feature of microporous ice films.

The vacancies denote the tendency to form hydrogen bonds with incident molecules, as a consequence of the highly polarized surface. Consequently, an incident molecule with a hydrogen bond receptor or donor group such as HCl will have a higher probability of sticking to the surface and leading to hydrogen bond formation.

Two kinds of dangling bonds are signified by a doublet at 3720 and 3696 cm^{-1} in low-density amorphous ice deposited below 15 K, and at 2748 and 2727 cm^{-1} for D_2O as shown in Figure 3.[13,14]

(a) Dangling O-H belonging to 3-coordinated molecules, with two hydrogen bonds via O and one via H, which gives rise to the low frequency form

(b) Dangling O-H belonging to 2-coordinated molecules, with one hydrogen bond via O and one via H which gives rise to the high frequency form.[14]

The higher and lower frequency features of each doublet have been assigned to 2-coordinated and 3-coordinated water molecules respectively.[14]

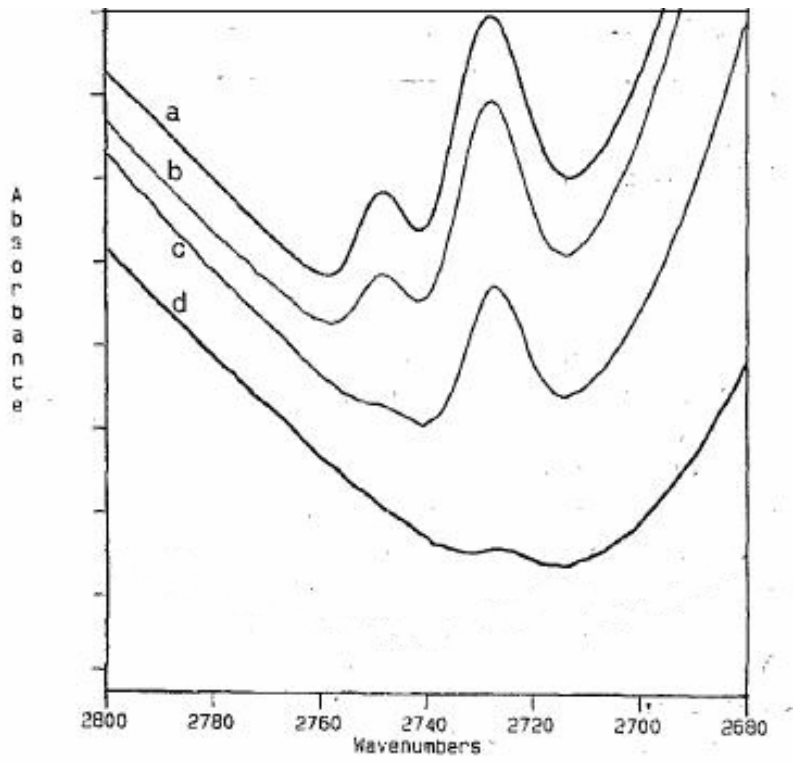

FIG.3. Infrared spectra of thin films of amorphous ice in the OD stretching mode region:

(a) Pure D_2O at 15 K

(b) unexchanged 50% D_2O / 50% H_2O at 15 K

(c and d) sample of part b annealed 10 min at 60 and 120 K

Adapted from Rowland *et al.*[13]

Buch and Devlin[14] reported that, upon annealing the amorphous ice film to 60 K, the 2-coordinate high-frequency component of the doublet was entirely diminished. However, the low-frequency component continued to remain in place. When amorphous ice is further annealed to 120 K, all evidence of the dangling OH disappears entirely. This disappearance is a consequence of the surface restructuring that take place alongside the annealing process, which leads to a reduction in the amount of internal surface in the solid ice. Similar results are exhibited by the spectra for the OD-stretching mode, and its IR absorption features are presented in Figure 3 as a function of both temperature and fraction of D_2O.

2. 2. 2. 1 Temperature and pressure dependence of the dangling OH bond

The temperature and pressure dependence of the IR absorption features are imperative to understand the formation of microporous ice at low temperatures and the collapse of micropores during annealing at 120 K.[13] The collapse of the micropores accompanies the densification and a change in the structural organization of the water ice network.[10] The temperature dependence of the dangling OH bond signifies that there are two regions for structural transitions in vapor-deposited ice that corresponds approximately to the regions where the density changes rapidly. Hence, the spectral feature of the dangling OH bond can also be used as a means to investigate the surface properties of water ice.

In the ballistic deposition model of ice, the incident H_2O molecules are deposited on the ice surface with a sticking probability of one, as they encounter unoccupied sites.[15] H_2O desorption is negligible at temperatures below 140 K.[10] Hence, an incident H_2O molecule brought to the water ice surface will be either buried by a successive inward-bound H_2O molecule or may diffuse to an unoccupied site in the ice multilayer. The time available for the admolecules to diffuse before they are buried by the H_2O layer is dependent on the incident H_2O flux.[10] At a high vapour deposition pressure, molecules are buried faster than they can diffuse. As the temperature decreases at a fixed deposition rate, it is less likely that a given molecule will have sufficient energy to the find a more favourable site in the network. If the molecule is buried in a higher orientation, more micropores and dangling bonds result within the ice bulk.[15]

2. 2. 3 Interaction with other species

Tielens *et al.*[9] conducted an extensive study on the interaction of amorphous ice with other species. The spectroscopic properties of water ice undergo changes upon interaction with impinging molecular species. Adsorbent species may alter the structure of amorphous solid water, based on factors such as their size, shape, and hydrogen bonding ability. Due to the existence of impurities, the degree of intermolecular coupling becomes smaller, and the hydrogen bonds become weaker because of increased O-O separation.[9,16] This phenomenon leads to an increase in the OH-stretching frequency and a decrease in librational and bending frequencies. In addition to these changes, the OH-stretching band

was reported to have become less intense as a result of the reduction in induced polarization. [9,16]

2. 2. 4 Species with incomplete hydrogen bonding

Molecules that are incident on the ice surface and that show deficiencies in forming hydrogen bonds can be identified by distinguishing features observed in the IR absorption spectra. [9,17] The following features can be seen as a result of the incomplete hydrogen bonding in the H_2O network as given in Figure 4:

(a) The terminal OH group in the water molecule can be identified by a distinct OH-stretching frequency around 3700 cm^{-1} in the presence of dilutant molecules that are incapable of accommodating hydrogen atoms to form hydrogen bonds (e.g., CH_4, Ar, O_2 or CO).

(b) The main OH-stretching band yields a shoulder at 3220 cm^{-1} when water molecules do not accept any H atoms at the O atom lone pair, but are able to donate H atoms to form hydrogen bonds (e.g., C_6H_6, C_2H_2).

Since H_2O molecules which do not accommodate hydrogen atoms are able to position themselves in a complementary placement to form hydrogen bonds, the 3220 cm^{-1} peak is observed at a lower frequency than that of the main OH stretching band.[9,16] The structural disparities of the dilutant species in terms of shape and size will result in dissimilarities in

their interaction with pure amorphous ice. These differences have been determined to increase in the order of CH_4, Ar, O_2 and CO.[9]

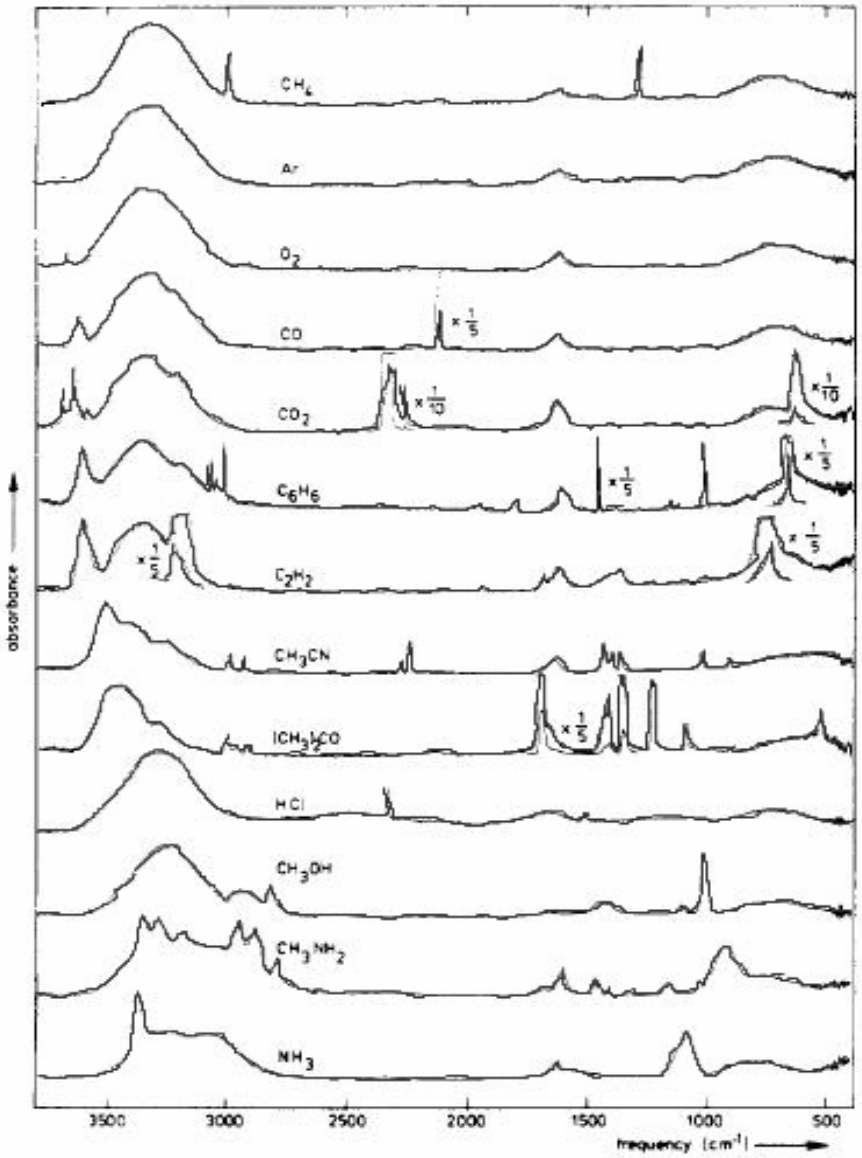

FIG.4. Infrared absorbance spectra of unannealed (10 K) binary mixtures of H_2O (mole fraction 33 %) and other components (66 %).

Adapted from Tielens *et al.*[9] . Line intensity has been increased for clarity.

2. 2. 5 Bases, Acids and Amphoteric molecules

Dilution of H_2O with hydrogen bonding molecules alters the H_2O IR absorption spectrum. Consider an incident molecule 'B' with the ability to donate electrons to create hydrogen bonds (e.g. NH_3). Such a molecule is considered to have characteristics of a base according to the Bronsted and Lewis concepts of acids and bases.[9]

The IR absorption features in H_2O change when such a molecule donates electrons to the H_2O network. A new hydrogen bond, O-H···B, is observed in the H_2O network.[9] In the case of a weak base, the HOH···B bond is weaker than the existing HOH···OH_2 bond. Such molecules will be distinguished by an OH-stretching frequency found between the main OH-stretching band of fully hydrogen bonded H_2O molecules and the 3700 cm^{-1} band of the free OH groups.[9,17] Hence, the spectral signature of a weak base is comparable to a non-bonding incident molecule.[9]

With increasing base strength, the OH-stretching frequency of these molecules will decrease, and the librational and bending frequency will increase.[9] The intensity of the OH-stretching frequency also increases due to two factors. Firstly, the strong base pulls more H_2O molecules out of the H_2O network than weak bases do. Secondly, when the O-H···B bond is strong, the polarization induced by the base causes an increase in the intensity of OH-stretching vibration in every H_2O molecule that forms a hydrogen bond

with the base.[9] The spectra of mixtures of H_2O and strong bases such as CH_3NH_2 and NH_3 reflect this behavior.[9]

Consider an incident molecule HA with the ability to donate hydrogen atoms and accept electrons to create hydrogen bonds. Such a molecule is considered to have characteristics of an acid according to the Bronsted and Lewis concepts of acids and bases (e.g. HCl). 'A' is a conjugate base of the acid HA and will form a hydrogen bond $O^{\cdots}H$-A. In this case, the hydrogen atom accepting the H_2O molecule acts as the base.[9] The conjugate base 'A' competes with H_2O for the hydrogen atom.

If the H_2O…HA bond is stronger than the $HOH^{\cdots}OH_2$ bond, the weakening of the bonds in the H_2O network causes the OH-stretching mode to shift to a lower frequency, while the frequencies of libration and bending increase.[9,16] In the case of weak acids, this process will lead to incompletely hydrogen bonded H_2O molecules in the H_2O network. This incomplete bonding will cause the 3220 cm^{-1} shoulder to increase. Tielens *et al.* observed that the 3220 cm^{-1} shoulder will disappear if the strength of the hydrogen bonds between H_2O and the acid is equal to that between two H_2O molecules.[9]

An incident molecule with the capacity to donate hydrogen atoms, as well as accept hydrogen atoms to form hydrogen bonds, is characterized as an amphoteric. The effect of an amphoteric on the H_2O spectrum will be a grouping of the characteristics explained above.[9] For example, methanol has amphoteric character like water and causes small

changes in the H_2O spectrum mainly due to the disruption of the hydrogen bonded network.

2. 3 Amorphous Solid Water

The chemical and physical characteristics of amorphous water ice are greatly affected by the microporosity in its structure. The total gas absorption area formed in the amorphous solid as a result of microporosity can reach several hundred m^2/g for ice grown at temperatures below 100 K.[3] Thus a fresh ASW surface is analogous to a high-capacity vacuum pump. As Baragiola[3] notes, "this pumping ability and long exposure times mean that icy surfaces in the solar system may be saturated with atmospheric gases." Unfortunately, the high porosity and strongly hydrogen bonded surface also means that in the case of experiments, contamination with background gases will be difficult to avoid.

2. 3. 1 Vapor deposition methods

A fundamental problem in studies of vapor-deposited ice has been that widely varying values have been reported for physical properties of ice, such as density, porosity, thermal conductivity, and effective area for gas absorption.[20] Stevenson *et al.*[15] suggested that these discrepancies in the literature concerning ASW may be due to differences in the morphologies obtained by a variety of deposition methods. They reported that the angular

distribution of incident H_2O flux used to grow the ASW films in a vacuum is a critical factor influencing the ASW morphology at low temperatures. They demonstrated that, by systematically varying the incident angle of the H_2O flux during deposition, the controlled growth of nonporous to highly porous ASW could be achieved.[15]

In astrophysical environments, the morphology of ASW will depend on the two possible mechanisms of formation: (a) direct deposition and (b) omni-directional deposition. Direct deposition may occur in the rings of Saturn, where it has been reported that water molecules sputtered from the outer rings accumulate on the inner rings; it may also occur when a body such as a dust grain is passing through a molecular cloud with a large relative velocity.[21] Porous ASW may form by means of omni-directional deposition of water molecules and may occur during the formation of comets.[21] In the light of these occurrences, the morphology of thin ASW films has been investigated by two different methods: [18]

(a) Using highly collimated effusive H_2O beams (i.e., "direct deposition")
(b) Introducing water vapor through a leak valve (i.e., "background deposition")

Kimmel *et al.*[18] observed that beam-deposited ASW films had an area of uniform thickness surrounded by an area of decreasing thickness, contained within the diameter of the sample. The films grown by ambient vapor were uniform across the sample.

Stevenson *et al.*[15] compared the N_2 adsorption of ice films varying in thickness, grown using both of these methods between 22 -145 K by dosing at different incident angles. For large incidence angles, the N_2 adsorption increased almost linearly with thickness, as given by Figure 4. The N_2 adsorption of ASW films grown by the background deposition method was higher than the adsorption of ASW films grown by collimated H_2O beams at high angles of incidence. The linear increase of the N_2 adsorption is indicative of the highly inter-connected pore structure that allows N_2 to penetrate the ASW film. Stevenson *et al.*[15] reported that the N_2 adsorption on ASW ice films grown at normal incidence was much smaller and almost independent of thickness. Moreover, they found that the ASW behaved as a denser film without a network of pores and that adsorption mainly took place through the external surface. The results were in agreement with the ballistic deposition model, which considers the effects of coarseness in the surface caused by random vapor deposition.

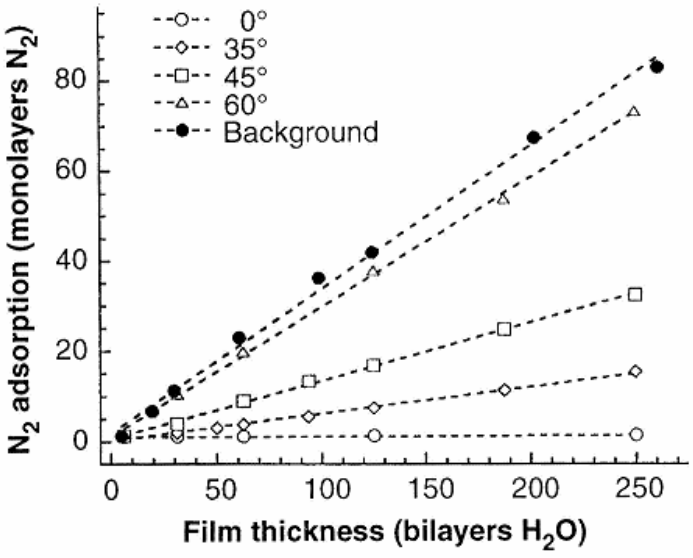

FIG.5. Amount of N_2 adsorbed by ASW films versus film thickness. The films were deposited by collimated beams at 22 K at the angles indicated; also shown are data for ASW films grown using background H_2O dosing. Fitted lines show a linear increase in N_2 uptake with increasing film thickness.

Reproduced from Stevenson *et al.*[15]

Stevenson *et al.*[15] also measured the N_2 adsorption by 50 bilayer ASW ice films as a function of the sample temperature, as given by Figure 6. They found that N_2 adsorption decreased with rising surface temperature. For ASW ice films grown at normal incidence, this decrease was small, since these are nonporous films independent of growth temperature. In contrast, for ASW ice films grown at oblique angles or by background deposition, N_2 adsorption is highly dependent on growth temperature. They observed an

extraordinarily large surface area of 2700 m^2/g at 22 K and 640 m^2/g at 77 K for ASW films grown from background deposition and reported a linear increase of porosity with time. With these observations, they proposed that large surface areas observed at low temperatures and oblique angles of the incident were a result of the connection of the internal surface being connected to the external surface of the film through a network of pores.

The porous character of low-density amorphous ice is caused by thermo-kinetic deposition. The incoming water molecules that adsorb at the surface may lose most of their energy well before finding the most stable site.[9]

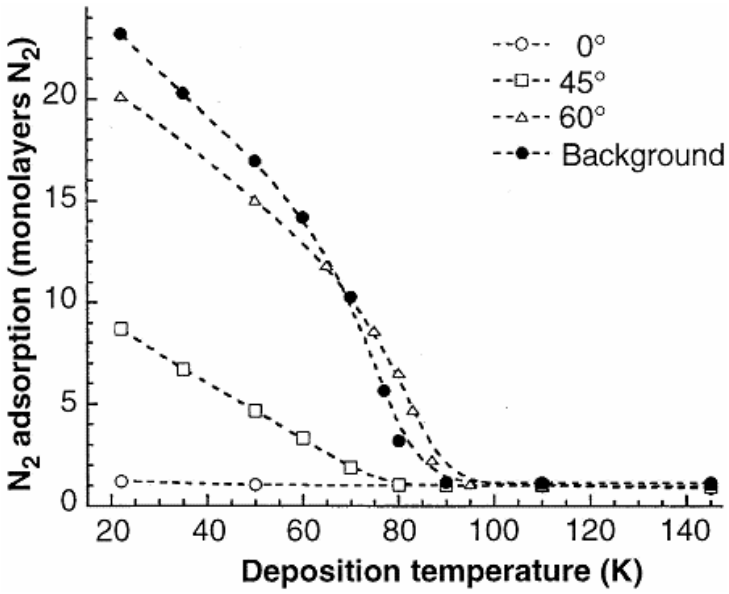

FIG.6. Amount of N_2 adsorbed versus growth temperature for 50-bilayer ASW films. The films were deposited by collimated beams at the angles indicated; also shown are data for ASW films grown using background H_2O dosing. The dotted lines through the data are to guide the eye. For the thin films and low deposition rates used in these experiments, the ASW film temperature and the Pt(111) temperature are essentially identical (Δ T<< 0.1 K).

Reproduced from Stevenson *et al.*[15]

2. 3. 2 Micropores

Vapor-deposited ice at 12 K grows with an extremely uneven surface that results in a microporous network with 5-10% of the molecules on the ice surface.[22] When water molecules incident on the ice surface have inadequate time to move to a suitable site before being covered by subsequent adlayers, they are buried in random orientations and leave gaps within the bulk ice. As a result, microporous networks are formed in the ice film. When these gaps are of a sufficient width, they prevent the formation of hydrogen bonds across the pore. Hence, 3-coordinate OH groups that are non hydrogen bonding are formed at the pore surface.[23] Devlin and Buch[22] observed the loss of surface OH vibrational signature between temperatures of 30 - 60 K. They proposed that the weakening of the IR absorption signal for dangling OH groups was a consequence of the solid water structure becoming less dense as the water molecules achieve a fuller co-ordination. This process yields an open tetrahedral network.[22]

Zondlo *et al.*[23] investigated the behavior of dangling OH bonds in vapor-deposited ice between 90 and 120 K and reported that the intensity of the dangling OH feature increased linearly with the thickness of the ice film. They proposed that the majority of the dangling OH was formed on the micropores of ice inside the condensed ice bulk. In addition, they suggested that low substrate temperatures and fast deposition rates led to the profusion of micropores in the condensed ice network.

Microporosity is related to the retention of gas in amorphous ice. Studies of gas adsorption on vapor-deposited amorphous ice have revealed that the amount of gas uptake is consistent with microporosity and large surface areas of up to hundreds of m^2/g. However, parameters such as pore shape, structure, and adsorption energies remain unknown.[24, 25]

In a study on the characteristics of pores using gas adsorption isotherms, Raut *et al.*[24] reported the existence of dual pore structure in the form of mesopores and micropores. They observed that the CH_4 adsorption isotherms for ice films formed by background deposition of water vapor were different from those for collimated beams. Films formed by background deposition demonstrated a step in the isotherms and less adsorption at low pressures. This observation led them to propose that the micropores formed by these two methods were dissimilar. In addition, they reported that films deposited at 77° incidence to the surface from a collimated beam developed both micro and mesopores. Upon annealing to 140 K, where the ice crystallizes, the micropores were destroyed while the mesopores were sustained.

2. 3. 3 Trapping of gas

The studies on the ability of water ice to trap and release gas have important implications linked to the outgassing process of comets.[24-27] These studies help characterize the pores connected to the outside of the ice but not the enclosed pores.[3]

Gases can be trapped by condensation on the ice surface at low temperatures below gas freezing temperature, or by the formation of clathrate hydrates in which the gas molecules are trapped in cages formed in the water ice only in the presence of the gas.[26,27] The high porosity of the amorphous ice allows large volumes of gas to settle in the vast number of cracks and holes. When the volume is filled and a monolayer of adsorbed gas is formed, the surplus gas freezes on the ice surface.[26]

Bar-Nun *et al.*[27] reported that CO, CH_4, N_2 and Ar gases trapped in are released at four temperature ranges:

(a) 30- 60 K: some of the holes are reopened and the gas frozen on water ice evaporates, while from 80- 120 K the annealing locks gas inside a compact and impermeable matrix.

(b) 135- 155 K: the trapped gas is squeezed out during the transformation from amorphous into less porous cubic ice.

(c) 160- 175 K: deeply buried gas is released during the transformation of cubic ice into hexagonal ice.

(d) 165- 190 K: gas and water are released simultaneously, during the evaporation of a clathrate-hydrate.

With increasing growth temperature, the gas absorption ability or porosity decreases greatly.[15]ASW formed at temperatures below 90 K is a highly adsorbent solid with a surface area of approximately 400 m^2/g.[28] At temperatures above 90 K, Stevenson *et al.*[15] observed that ASW films essentially had the same adsorption as the non porous

crystalline ice formed at 145 K. Rowland *et al.*[13] reported that dangling O-H bonds diminished by warming to temperatures near 60 K. They concluded that micropores that continue to remain in ice above 60 K have no access to the surface.

In a study on the gas retention of ASW, Baragiola[3] reported that ~1.7 nm cavities in ASW disappear or join together at 100 K, but some cavities continue to remain even after warming beyond the crystallization temperature.[29] Upon annealing ASW becomes a compact solid with closed pores and this yields a reduction in gas adsorption.[3,24] Horimoto *et al.*[30] investigated methane adsorption using infrared spectroscopy and proposed that gas adsorption was rendered by cavities larger than micropores which collapse upon annealing to 60 K. They concluded that micropores are not affected until 80 K and collapse only at 120 K.

2. 4 Photolysis of ASW

The effects of ultraviolet radiation on water ice are important in the chemistry of both atmospheric and interstellar ices. Significant progress has been made in understanding the chemical and physical processes following the absorption of Ultraviolet (UV) photons by condensed phases of water.

Cosmic dust is formed from gases of refractory elements such as Mg, Si, O and C around 1000 K.[4, 32-34] Dust diffuses to interstellar space and gradually forms a molecular cloud.

Herbst[33] has reported extensively on the formation of molecular clouds. Watanabe *et al.*[4] reported that a significant amount of radiation penetrates through relatively thin molecular clouds since their inception. As a result of photoerosion, volatile molecules cannot remain stable at the surface of the molecular cloud. Hence, dust is found as bare silicate or carbonaceous particles in the molecular cloud.[4] The temperature of the molecular cloud begins to lessen as the density of the dust particles increases. This process is followed by a reduction in the photon field due to optical absorption.[4]

A presolar molecular cloud[33] is formed when a molecular cloud is cooled from 1000 K to 10 – 100 K. Due to the exceeding reduction in the photon field, atoms and molecules deposit on the dust surfaces and can now form a solid ice mantle.[4] At the end of this process a presolar molecular cloud contains dust consisting of core-mantle particles and an additional outer mantle of volatile ices dominated by H_2O as given in Figure7. [33]

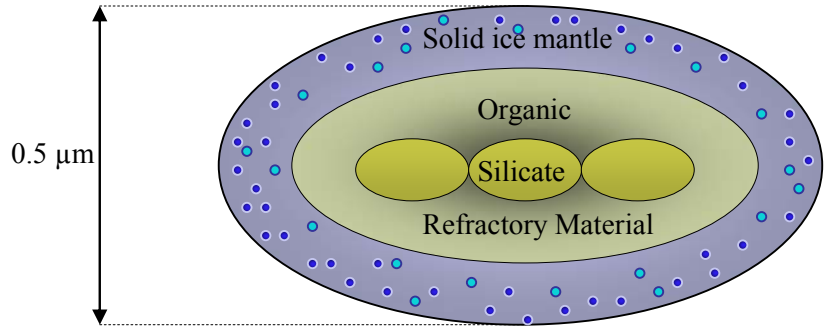

FIG.7. Structure of a cosmic dust particle. Adapted from Herbst.[33]

Over 120 molecular species of ions and complex organic molecules have been detected in molecular clouds. These species evolve from atoms and other simple molecules through surface mediated chemical reactions.[4,33,34] Almost 50 percent of the species found in molecular clouds are familiar terrestrial species such as water, ammonia, formaldehyde, and simple alcohols such as methanol and ethanol.[33] The other 50 percent of the species include positive ions (e.g. H_3^+, HCO^+, H_3O^+), radicals (e.g. C_nH through $n = 8$), isomers of stable compounds (e.g. HNC, HCCNC, HOC^+), and unusual three-membered rings (e.g. C_3H, C_3H_2).[33] Of course, molecular hydrogen is found to be the dominant species.[32-34] The second most abundant species is CO.[33] The concentration of molecular hydrogen is reported to be 10^4 times higher than that of CO.[33]

Chemical process on ice mantles can be categorized into two types:

(1) Energetic processes caused by radiation.

(2) Non energetic surface reactions in which abundant atoms such as hydrogen and oxygen play an important role.[4]

Photons in the range from UV to Vacuum Ultraviolet (VUV) can induce chemical reactions on ice mantles. Dust shielding a dense molecular cloud makes it difficult for UV and VUV photons to penetrate the cloud.[4,31] The internal UV flux in a dense cloud is approximately 10^3 photons cm^{-2} s^{-1}.[35] Although this flux gives one incident photon per month on a grain, a significant chemical evolution takes place over the life time of a molecular cloud, which is 10^6-10^7 years. Hence, certain processes induced by UV absorption are important in evolving molecular clouds.[31]

Within the characteristic temperature range of 10-100 K in molecular clouds, molecules are typically synthesised through barrier-less ion-molecule reactions in the gas phase and therefore these gas phase reactions have been studied over a long period.[4,31-34] However, the insight that the profusion of some molecules such as hydrogen molecules cannot be explained by pure gas phase formation has drawn considerable attention to the surface reactions on dust grains which account for the formation of these molecules.[4]

The cosmic ray ionization of hydrogen molecules produced on grains and desorbed into the interstellar gas is indicated below.[33]

$$H_2 + \text{cosmic ray} \rightarrow H_2^+ + e^- + \text{cosmic ray} \qquad (1.1)$$

H_2^+ ion reacts with molecular hydrogen to produce H_3^+.[33]

$$H_2^+ + H_2 \rightarrow H_3^+ + H \qquad (1.2)$$

The H_3^+ ion is a comparatively abundant species as it does not react with molecular hydrogen.[33] Hence, the H_3^+ ion serves as a precursor for gas phase reactions in the molecular cloud with its ability to react with other species.[33] For example, the reactions with atomic oxygen initiate a chain of reactions leading to the production of the hydronium ion via reactions (1.3), (1.4), and (1.5).[33]

$$H_3^+ + O \rightarrow OH^+ + H_2 \qquad (1.3)$$

$$OH^+ + H_2 \rightarrow H_2O + H \qquad (1.4)$$

$$H_2O + H_2 \rightarrow H_3O^+ + H \qquad (1.5)$$

Besides gas phase reactions, in the cold region of the molecular clouds where dust grains are covered with the water ice mantle, H_2 production through the photolysis of H_2O molecules in icy mantles is important. Yabushita *et al*.[36,37]measured kinetic energy and the rovibrational population of H_2 molecules produced by 157 nm photolysis of water ice at 100 K using the REMPI method. When water ice is exposed to VUV radiation, the H-O bond ruptures, and this is reported as a photolytic source of hot hydrogen atoms at the surface of comets and dust grains in the interstellar medium.[38] Yabushita *et al*.[36,37] reported that hydrogen molecules on ASW are produced by two distinct mechanisms: hydrogen abstraction [*HAB*, reaction (1.6)] and hydrogen recombination [*HR*, reaction (1.7)].

$$HAB: H + HOH \rightarrow H_2 + OH \quad (1.6)$$

$$HR: H + H \rightarrow H_2 \quad (1.7)$$

Since the optical penetration depth of a water ice film at 157 nm is ~100 nm, Yabushita *et al*.[36,37] proposed that H atoms produced far beneath the ice surface will collide with surface OH groups that are exposed through the porous surface of ASW to produce hydrogen molecules.[36,37]

Andersson *et al.*[31] reported that, unlike in a molecular cloud, multiple photodissociative events can take place on the water ice surface within a narrow range of time and space when exposed to a high flux of UV photons. Photofragments released from different sites

can react with one another to produce species such as OH, HO_2, O_2 and H_2O_2.[31] Some photofragments are observed to be mobile and may move distances of several angstroms before becoming trapped in sites and they can partake in additional reactions. However, the recombination process such as the reaction of H and OH to form H_2O limits the possibility of the photofragments reacting further.[31]

The presence of OH, HO_2, and H_2O_2 products in UV photolysis of ice deposited on solid Ar has been observed by Gerakines *et al.*[35] The photochemistry of the water molecule is initiated by reaction (1.8).

$$H_2O + h\upsilon \rightarrow H + OH \qquad (1.8)$$

Subsequent steps lead to the production of H_2O_2 and HO_2 as given in reactions (1.9) and (1.10).[35]

$$OH + OH \rightarrow H_2O_2 \qquad (1.9)$$

$$OH + H_2O_2 \rightarrow H_2O + HO_2 \qquad (1.10)$$

H_2O_2 has been observed as a minor component of the water ice on the surfaces of Europa, a satellite of Jupiter and of Enceladus, one of Saturn's icy moons.[39] The UV photolysis of nitrate on snow grains produces H_2O_2, which is reported as a precursor for the production of OH in polar air through secondary photolysis.[40] In a study on the formation of H_2O_2 at the ice surface following the photodissociation of ASW at 90 K, Yabushita *et al.*[40] proposed a mechanism for this process via reactions (1.11)-(1.13).

$$H_2O + h\upsilon \rightarrow H + OH \qquad (1.11)$$

$$OH + OH \rightarrow H_2O_2 \quad (1.12)$$

$$H_2O_2 + h\upsilon\,(300 - 350\ nm) \rightarrow 2OH \quad (1.13)$$

Molecular dynamics calculations performed by Andersson *et al.*[31] to simulate the photodissociation of water ice at 10 K, showed that OH radicals move at most 5 Å through bulk ice. However, OH radicals released from photodissociation at the surface were reported to be highly mobile with the ability to travel 80 Å over the surface.[31] Since there is appreciable mobility at 90 K, the distance between many OH radicals will be comparable with their bimolecular reaction radius so that OH recombination reactions can produce H_2O_2 on the ice surface.[40]

In addition to the UV initiated reactions of water ice, the heterogeneous reactions that take place on water-ice particles have attracted considerable attention as well. The molecular adsorption on ASW is significant in environmental chemistry.[12] For example, the release of oxygen atoms into the atmosphere from NO_3^- adsorbed on ice is important in the formation of ozone and in the cycling of NO_x in the Arctic and Antarctic boundary layer.[41-44] Davis *et al.*[41] reported that the summertime boundary layer over the South Pole has elevated levels of NO_x, OH and O_3. Nitrate plays an important role in snowpack photochemistry as the precursor for the formation of these oxidizing species as given in reactions (1.14-1.16).[45]

$$NO_3^- + h\upsilon\,(340\ nm) \rightarrow O(^3P) + NO_2^- \quad (1.14)$$

$$NO_2^- + h\upsilon + H^+ \rightarrow NO + OH\ /\ HONO \quad (1.15)$$

$$NO_2 + h\upsilon \rightarrow O(^3P) + NO \quad (1.16)$$

Yabushita *et al.*[45] have detected the formation of the oxygen atom via reaction (1.16) and have reported that these reactions play a central role on air pollution at the South Pole.

Many CO-bearing molecules, including simple organic molecules such as H_2CO and CH_3OH, have been discovered abundantly in the ASW mantle of dust grains.[35,46] These molecules serve as important precursors to form complex organic molecules. They require the chemical processes through surface reactions to produce the observed abundances.[4] Since CO exists abundantly on the dust surface, these molecules are considered to evolve from it. Chapter 5 of this thesis discusses in the photolysis of methanol ice.

2.5 Conclusion

Chemical reactions on the surface of cosmic ice dust play an important role in chemical evolution. Among the many kinds of molecules observed, the abundances of some major species such as hydrogen molecules cannot be explained by gas-phase synthesis. Therefore, surface reactions on cosmic dust are considered for the synthesis of such molecules. Further research on the reactions that takes place on the water ice surface is desirable in order to understand the formation and evolution of icy grains in molecular clouds.

References for Chapter 2

[1]M. A. Tolbert, A. M. Middlebrook, J. Geophys. Res., **95**, 22423 (1990).

[2]P. Jenniskens and D. F. Blake, Astrophys. J. 473, 1104 (1996).

[3]R.A. Baragiola, Planet. Space Sci. **51**, 953 (2003).

[4]N. Watanabe, and A. Kouchi, Prog. Surf. Sci. **83**, 439 (2008).

[5]A. H. Narten, C. G. Venkatesh, and S.A Rice, J. Chem. Phys. **64**, 3 (1976).

[6]C. A. Angell, Annu. Rev. Phys. Chem. **55**, 559 (2004).

[7]S. Mitlin and K.T Leung , J. Phys. Chem. B **106**, 6234 (2002).

[8]P. Jenniskens, and D. F. Blake, Science **265**, 753 (1994).

[9]A. G. G. M. Tielens, W. Hagen, and J. M. Greenberg, J. Chem. Phys. **87**, 4220 (1983).

[10]B. S. Berland, D. E. Brown, M. A. Tolbert, and S. M. George, Geophys. Res. Lett., **22**, 3493 (1995).

[11]W. Hagen, A. G. G. M. Tielens, and J. M. Greenberg, Chem. Phys. **56**, 367 (1981).

[12]S. Sato, D. Yamaguchi, K. Nakagawa, Y. Inoue, A. Yabushita, M. Kawasaki, Langmuir, **16**, 9533 (2000).

[13]B. Rowland, and J. P. Devlin, J. Chem. Phys. **94**, 812 (1991).

[14]V. Buch, and J. P. Devlin, J. Chem. Phys. **94**, 4091 (1991).

[15]K. P. Stevenson, G. A. Kimmel, Z. Dohnalek, R. S. Smith, and B. D. Kay, Science **283**, 1505 (1999).

[16]L. Schriver- Mazzuoli, A. Schriver, and A. Hallou, J. Mol. Struct. **554**, 289 (2000).

[17]S. Mitlin, K. T. Leung Surf. Sci. **505**, L227 (2002).

[18]G. A. Kimmel, K. P. Stevenson, Z. Dohnalek, R. S. Smith, and B. D. Kay, J. Chem. Phys. **114**, 5284 (2001).

[19]E. Mayer and R. Pletzer J. Chem. Phys. **80**, 2939 (1984).

[20]M. S. Westley, G. A. Baratta, and R. A. Baragiola, J. Chem. Phys. **108**, 3321 (1998).

[21]R. Smoluchowski, Science **201**, 809 (1978).

[22]V. Buch, and J. P. Devlin, J. Phys. Chem. **99**, 16534 (1995).

[23]M. A. Zondlo, T. B. Onasch, M. S. Warshawsky, and M. A. Tolbert, J. Phys. Chem. B **101**, 10887 (1997).

[24]U. Raut, M. Fama, B. D. Teolis, and R. A. Baragiola, J. Chem. Phys. **127**, 204713 (2007).

[25]A. Givan, A. Loewenschuss, and C. J. Nielsen, J. Phys. Chem. B **101**, 8696 (1997).

[26]A. Bar-Nun, G. Herman, and D. Laufer, Icarus, **63**, 317(1985).

[27]A. Bar-Nun, J. Dror, E. Kochavi, and D. Laufer, Phys. Rev. B, **35**, 2427 (1987).

[28]E. Mayer, and R. Pletzer, Nature, **319**, 298 (1986)

[29]M. Eldrup, A. Vehanen, P. J. Schulz, K. G.Lynn, Phys. Rev. B, **32**, 7048 (1985)

[30]N. Horimoto, H. S. Hiroyuki, and M. Kawa, J. Chem. Phys. **116**, 4375 (2002).

[31]S. Andersson, A. Al-Halabi, G.-J. Kroes and E. W. Dishoeck, J. Chem. Phys. **124**, 064715 (2006).

[32]M. Greenberg, and J. I. Hage, Astrophys. J. **361**, 260 (1990).

[33]E.Herbst, Chem. Soc. Rev. **30**, 168 (2001).

[34]L. J. Allamandola, S. A. Sandford, and G. J. Valero, Icarus **76**, 225 (1988).

[35]P. A. Gerakines, W. A. Schutte, J. M. Greenberg, and E. F. van Dishoeck, Astron. Astrophys. **296**, 810 (1995).

[36]A. Yabushita, N. Kawanaka, D. Iida, T. Hama, M. Kawasaki, N. Watanabe, M.N.R. Ashfold, and H.-P. Loock, J. Chem. Phys. **129,** 044501 (2008).

[37]A. Yabushita, N. Kawanaka, D. Iida, T. Hama, M. Kawasaki, N. Watanabe, M.N.R. Ashfold, and H.-P. Loock, Astrophys. J. **682**, L69 (2008).

[38]G. Manico, G. Raguni, V. Pirronello, J. E. Roser, G. Vidali, Astrophys. J. **548**, L253 (2001).

[39]R.W. Carlson, M. S. Anderson, R. E. Johnson *et al.*, Science **283**, 2062 (1999).

[40]A. Yabushita, D. Iida, T. Hama, and M. Kawasaki, J. Chem. Phys. **129,** 014709 (2008).

[41]D. D. Davis, J. B. Nowak, G. Chen, M. Buhr, R. Arimoto, A. Hogan, F. Eisele, L. Maudlin, D. Tanner, R. Shetter, B. Lefer, and P. McMurry, Geophys. Res. Lett. **28**, 3625 (2001).

[42]R. Weller, A. Minikin, G. Konig- Langlo, O. Schrems, A. E. Jones, E. W. Wolff, and P. S. Anderson, Geophys. Res. Lett. **26**, 2853 (1999).

[43]A. E. Jones, R. Weller, A. Minikin, E. W. Wolff, W. T. Sturges, H. P. McIntyre, S. R. Leonard, O. Schrems, and S. J. Bauguitte, J. Geophys. Res.-Atmos. **104**, 21355 (1999).

[44]A. E. Jones, E. W. Wolff, J. Geophys. Res.-Atmos. **108**, 4565 (2003).

[45]A. Yabushita, N. Kawanka, M. Kawasaki, P. D. Hamer, and D. E. Shallcross, J. Chem. Phys. **129,** 014709 (2008).

[46]S. Malyk, G. Kumi, H. Reisler and C. Wittig, J. Phys. Chem. A **111**, 13365 (2007).

Chapter 3
Velocity Map Imaging and Simulations

3.0 Introduction

The technique of ion and electron imaging has become an indispensible tool in the study of chemical dynamic processes such as bimolecular reactions, photodissociation, and photoionization.[1-6] Imaging techniques allow three-dimensional (3D) angular and velocity distributions of the products formed from photolysis to be visualized directly. In this chapter, the developments in velocity map imaging will be reviewed, the characteristics of the velocity map imaging spectrometer will be discussed using the Simion 7.0 software package, and the simulation of the experimental image of ionized photoproducts will be illustrated using Microsoft Visual Basic 6.0.

The earliest study on "Photolysis Mapping" was reported by Solomon[7] in 1967. He investigated the photolysis of bromine and iodine molecules in a glass hemisphere coated with tellurium, with polarized light emitted from a mercury lamp. Upon photolysis, the halogen photofragments removed the tellurium in the photolysis cell, and created an anisotropic depletion pattern. This first visualization of the spatial distribution of photofragments led to the evolution of ion imaging techniques.

Chandler and Houston[8] marked a phenomenal advancement in ion imaging 1987, when they combined use of position sensitive ion detection with Charge-Coupled Device (CCD) cameras to provide a more sensitive technique to investigate the photodissociation process. This technique was achieved by directing a skimmed CH_3I molecular beam through a hole in the repeller plate of the ion optics assembly. The molecular beam was then intersected by photolysis and probe laser beams at position between the repeller and the grounded grid electrodes. The photolysis laser ruptured the C-I bond at 266 nm, and produced CH_3 radicals and I atoms, while the probe laser ionized the $CH_3(\nu=0)$ photofragment.[8] The potential between the electrodes was controlled so that the resulting CH_3^+ ion cloud is accelerated through a Wiley-McLaren Time-of-Flight Mass Spectrometer (TOF-MS)[9] on to the detector. The electric field also compresses the CH_3^+ ion cloud along the time-of-flight axis and all ions arrive at the position sensitive detector concurrently.[10] This phenomenon, known as "pancaking," is crucial to minimize the blurring of the image.[11] The detector is composed of a position-sensitive Microchannel Plate (MCP) and a Phosphor Screen (PS). The three dimensional (3D) ion cloud is projected as a two-dimensional (2D) image on to the detector positioned at the end of the drift tube. The pattern of the ions striking the detector can then be captured by a CCD camera, and processed by using imaging software programs. The 3D ion cloud is projected as a 2D image on to the detector positioned at the end of the drift tube. The raw images may then be used to calculate the velocity and the kinetic energy distributions. [12]

The photofragments produced from photodissociation or photoionization depart with a fixed amount of kinetic energy (KE) as given in equations (2.1) and (2.2) respectively[1]:

$$AB + h\nu \rightarrow A + B + KE \quad (2.1)$$

$$AB + h\nu \rightarrow AB^{+} + e^{-} + KE \quad (2.2)$$

The kinetic energy is portioned among photofragments according to the conservation of momentum, as given in equations (2.3) and (2.4):

$$KE_A = \left(\frac{M_B}{M_{AB}} \right) \times KE \quad (2.3)$$

$$KE_B = \left(\frac{M_A}{M_{AB}} \right) \times KE \quad (2.4)$$

According to the mass portioning factor, the lighter particles carry the larger fraction of kinetic energy. Hence, in a photoionization reaction the electrons carry most of the kinetic energy, and in the photodissociation of a homonuclear diatomic such as H_2 the total kinetic energy is shared equally between the two H fragments produced.[1] According to conservation of momentum, each photodissociation reaction produces two partner fragments with equal momentum, flying in the opposite direction of the center-of-mass frame. These fragments are then able to create scattering patterns with a spherical distribution known as Newton spheres. For a diatomic molecule with the transition dipole moment that is aligned parallel to the polarization of the photolysis laser beam, the spatial distribution of photofragments assumes a $\cos^2\theta$ distribution, whereas a $\sin^2\theta$ distribution is produced if the transition dipole moment lies perpendicular to the bond. A

single photodissociation event AB + hν → A + B where mass A > mass B creates the Newton spheres shown in Figure 8. Over time, the photodissociation will produce two nested spheres with a radii ratio of

$$\frac{R_A}{R_B} = \frac{m_A}{m_B} \tag{2.5}$$

where the radius of each sphere is given by

$$R = \sqrt{\frac{2KE}{m}}t \tag{2.6}$$

when t is the time-of-flight.

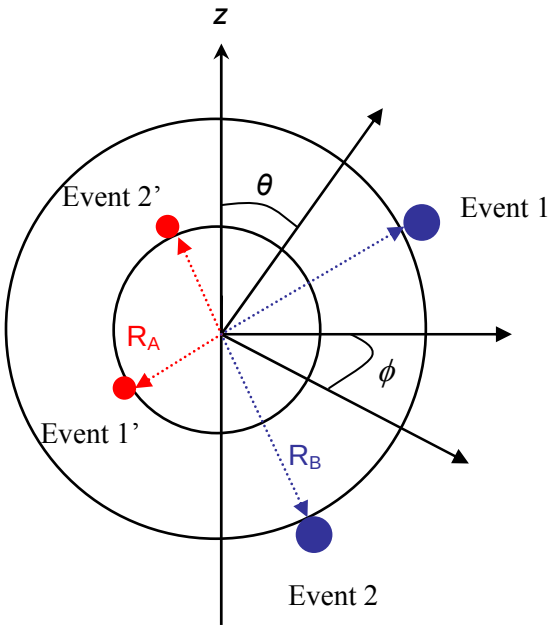

FIG.8. Nested Newton spheres photofragments A and B where $m_A > m_B$. The polar angle θ is defined with respect to the z axis, the azimuthal angle is ϕ, and the radius is given by R. Reproduced from Whitaker.[1]

Eppink and Parker[13] improved the original technique significantly in terms of spatial resolution when they replaced the conventional grid electrode assembly used in ion imaging with a three-plate electrostatic lens with open electrodes. They also introduced an additional extractor electrode to the ion optics assembly. Additionally, this lens system could be tuned so that the ions with the same initial velocity are mapped onto the same point on the detector, regardless of their initial spatial position.[13] Hence, this technique of ion lens optics and 2D imaging became known as "Velocity Map Imaging".[13] and has become an essential tool in many different fields. The typical imaging setup includes a pulsed molecular beam source; an ion optics assembly comprised of repeller, extractor, and ground electrodes; and an image detector as represented in Figure 9. The images produced using the ion optics assembly in ion imaging and velocity map imaging are compared in Figure 10. Furthermore, VMI improves ion imaging by magnifying the radii of the ion images. Eppink and Parker[13] defined this radius (R) as:

$$R = N v t \tag{2.7}$$

where v is the expansion speed, t is the time-of-flight, and N is a magnification factor that depends on the experimental setup and electric fields.

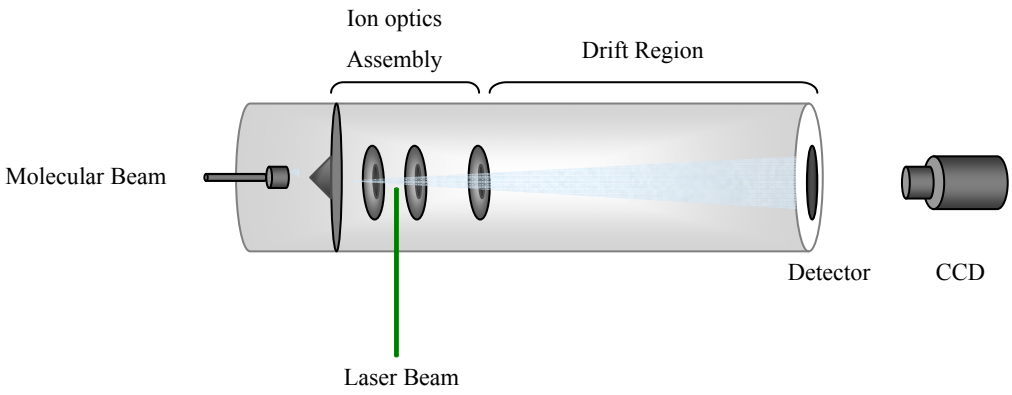

FIG.9. Schematic representation of the instrument set up in velocity map imaging.

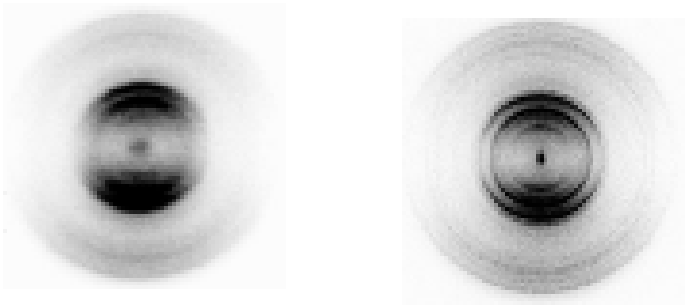

Ion imaging

Velocity map imaging

FIG.10. Comparison between images of O^+ ions from the photolysis of molecular oxygen at 225 nm.

Reproduced from Eppink and Parker. [25]

Chang *et al.*[14] made a significant contribution to the technique by improving the resolution of the images further. They analyzed each spot detected by the CCD camera where the burst of electrons created a blur in the image as a result of several pixels being excited, and eliminated this problem by introducing real-time event counting. The highest intensity pixel was selected and stored for each ion that struck the phosphor screen, so that the pixel values correspond directly to the number of ions detected at each pixel position.[11]

The raw images from the CCD camera are in fact 3D projections of Newton spheres on a 2D screen. In order to extract the kinetic energy and angular distribution information from the images, it is necessary to reconstruct the original 3D distributions. Suits *et al.*[15] have developed a method by which only the centre slice of the ion sphere is recorded and thereby circumvents these mathematical reconstruction methods. His DC-slicing method is used to stretch the ion sphere (rather than pancaking it) and the detector is only turned on when the centre fraction of the sphere arrives. This necessitates the use of additional electrodes and electric fields, but has been widely adopted, especially for heavier fragments. In addition, there are two fundamental approaches used in literature to reconstruct the 3D distribution from the projected full ion sphere:[15] (a) inversion methods[16] and (b) forward convolution methods.[1]

The inversion methods assume that if the 3D distribution has an axis of cylindrical symmetry, and if a 2D-central slice is taken through the 3D distribution, the slice contains

all the information required to reconstruct the original distribution.[1,16] From this slice, the 3D projection is obtained by rotation around the cylindrical axis – a process known as the Abel transformation. The inverse Abel transform can be used to obtain the slice from the projection of the 3D distribution.

In an experimental point of view in a photodissociation process, if the polarization of the photolysis laser is parallel to the plane of the detector, then the resulting photofragments will always possess an axis of cylindrical symmetry.[1] In such cases, the inverse Abel transform can be used to recover a central slice from the 3D distribution.[1] In cases where cylindrical symmetry is not observed, forward convolution or basis set methods are employed.[17-19] In the onion-peeling program published by Manzhos and Loock[20] , the velocity and angular distribution is determined by the back simulation of a raw image with user-defined parameters. Another approach based on Monte-Carlo type simulations is presented below.

3.1 Experimental Set Up

The velocity map imaging spectrometer consists of a high vacuum chamber, a pulsed laser system, and a particle detection system. The high vacuum chamber is typically evacuated to 10^{-7} Torr. The vacuum system consists of an ionization chamber and a TOF chamber that are evacuated using two turbo-molecular pump (Pfeiffer, TMU521 and

Varian TV701 navigator) backed by Edwards and Welch rotary pumps. The two chambers are connected by a sliding gate valve.

Gaseous samples are introduced to the vacuum chamber through a molecular beam valve. The molecular beam is expanded to the vacuum chamber with a cylindrical nozzle and is collimated by a 0.5 mm skimmer mounted 50-60 mm downstream from the nozzle. The molecular beam valve is powered by a pulse driver (General Valve, Iota One) that is synchronized by a LabVIEW program. The gaseous sample is then frozen on to a sapphire rod (Cryo industries) supported in the middle of the vacuum chamber. The sapphire rod is attached to a helium compressor (Sumitomo, Cryo Industries HC-4E), and has an Au (111) plated tip. The temperature of the sapphire rod is controlled in the range 8-120 K by a temperature controller and a sensor in the cold finger assembly.

Photofragments are produced from the frozen gas sample by laser photolysis of the ice matrix. They are detected through the (2+1) REMPI process using a second, delayed probe laser. The probe laser is a tunable and frequency doubled dye laser (Lambda Physik, Scanmate 2E: Dye Laser) that is pumped by a XeCl Excimer Laser (Lambda Physik, LPX-200,160-200 mJ/pulse) operating at 308 nm. The output beam from the dye laser in the probe laser system is frequency doubled using β-BaB_2O_4 crystal. Photolysis can be performed using either another dye laser (Lambda Physik, Scanmate 2E) pumped by an Nd: YAG laser (Continuum Powerlite Precision 8000, 532 nm), or by using an Optical Parametric Oscillator (OPO) unit pumped by an Nd: YAG laser (Spectra Physics,

355 nm). The output of the OPO unit can be tuned between 214-354 nm. The laser beams are perpendicular to the TOF axis and meet the molecular beam between the repeller and extractor electrodes.

Infrared spectra will be collected before and throughout the photolysis of the frozen gas sample with a commercial FT-IR spectrometer (Thermo Scientific Nicolet 6700). The FT-IR spectra allow the characterization of the ice matrix. Since FT-IR is used to study the water ice surfaces, the beam path has to be free of water vapor in the air. This has been achieved by using an acrylic housing for the beam path that is filled by gas from a purge gas generator.

The produced photoions are accelerated in a VMI field and drift through a flight tube (74 cm) onto the charged particle detection system. The charged particle detection system consists of a MCP (Chevron, Burle-Electro Optics Inc.) with a diameter of 75 mm, and a phosphor screen. Voltages are applied to the MCP to gate-selected ions using high-voltage power supply (Keithley Instruments 245 and 246). The images of the ions that strike the phosphor screen are detected using a CCD camera (Optikon, 12 bit, 1280 x 1024 resolution) and the images are read out and are stored in the lab computer. The schematic of the experimental set up is given in Figure 11.

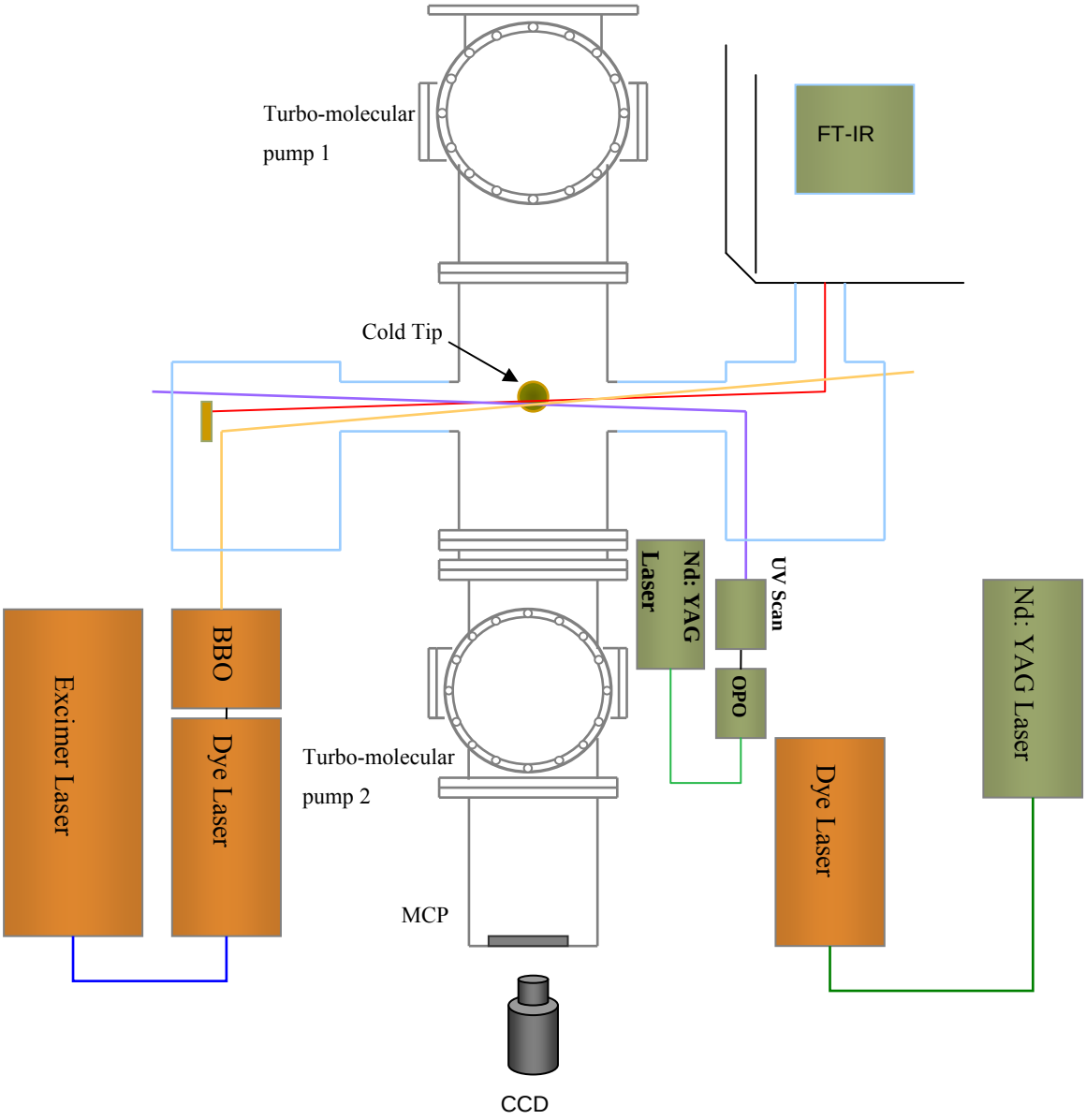

FIG.11. Top view of the experimental set up.

The studies on physical properties of cryogenic ices, especially related to ice surfaces, the phase transitions of ice, and the studies of matrix effects on the vibrational spectra of molecules have received significant attention in the recent years.[21-25] However, the properties of surfaces and the states of the adsorbed species have not been studied simultaneously. The combination of velocity map imaging to determine the kinetic energy and the angular distribution of the photoproducts, and FT-IR spectroscopy to determine the chemical composition of the ice matrix before and throughout photolysis, provide an optimized method to investigate the photochemistry of water ice and its constituents. The characteristics of the velocity map imaging spectrometer are important when acquiring the velocity profile of a photofragment.

In the following section, the characteristics of the velocity map imaging spectrometer are discussed through a simulation using the Simion 7.0 software package. The dependence of the resolution on the ion optics voltage is explored through this simulation. Additionally, a software program written using Microsoft Visual Basic 6.0 to simulate the experimental pattern observed on the position sensitive detector from the photoproducts is discussed in detail. These simulations provide useful information for estimates of resolution for experiments with other photoproducts.

3.2 SIMION Simulations

The mapping of the 3D distributions of the desorbed photofragments onto the 2D detector plane is dependent on the configuration of the electrostatic lens system in the TOF and the voltages applied to them. The TOF consists of three electrodes, namely repeller (R), extractor (E) and ground (G). These are used to accelerate the desorbed and resonantly ionized photofragments into a field-free drift region. Upon ionization, charged particles form one or several nested Newton spheres which collapse into two dimensions along the TOF axis for each particular mass.[13] In conventional TOF-mass spectrometers, ions of the same kinetic energy but with velocities in different directions arrive at the detector at different times. When the velocity map focusing conditions are met, ions of the same mass that were formed at a given time, with the same velocity, converge on the same point on the detector, regardless of their position of origin. Since the drift region of the TOF chamber is of fixed length, the convergence of the beam depends on the ratio of the voltages applied on the extractor and repeller (V_E/V_R).

The SIMION 7.0 software package[26] allows the calculation of ion trajectories that fly through 3D electrostatic fields that assume cylindrical symmetry. The SIMION virtual optics bench was used to simulate the three open-hole electrodes, each 11.4 cm in diameter, and a TOF chamber that is 74 cm long. The electrode geometries and potentials at each point in geometry are stored in a potential array, and the voltages applied to the

electrodes were then manipulated as required. The modeled spectrometer is given in Figure 12.

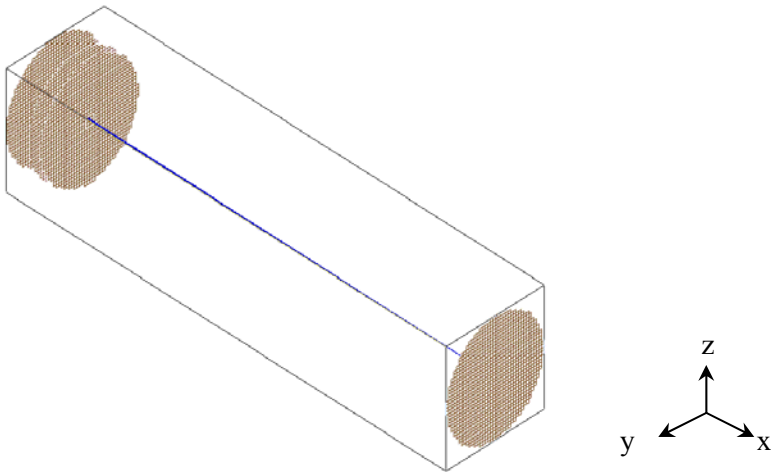

FIG.12. 3D TOF simulated by SIMION 7.0 with repeller, extractor, ground electrodes and detector.

Five ions of equal mass and without initial kinetic energy were generated in the region between the repeller and the extractor by first defining the position of the first ion and then incrementing the position of the others by 1 mm in the *y* direction, i.e., perpendicular to the TOF axis. The simulation was repeated for different voltage settings until the trajectories with the same initial velocity, but different initial positions, were converged to a single point on the detector. This is the "velocity mapping" condition. The optimal focusing voltage for V_E/V_R was found to be 0.55075. After setting the extractor voltage division "in focus" the setup is ready to collect ion and electron images that do have

kinetic energy release.[13] If the laser position and V_E/V_R ratio are kept the same, the only variable is the repeller voltage (V_R) to obtain images in the size that is desired. Now images of any ion mass can be obtained without having to change the V_E/V_R ratio.[13] This simulation is illustrated in Figure 13.

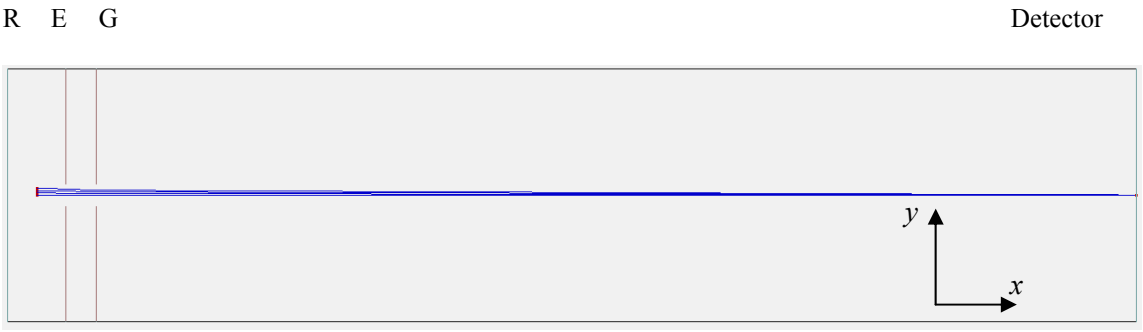

FIG.13. The *xy* plane view of the simulated TOF. When V_E/V_R meets the focusing condition, all ionized species with the same mass and the same velocity reach the MCP detector regardless of the location they were formed.

In the next simulation, given in Figure 14, the magnification factor for the image was calculated. The magnification factor is the factor by which the total image size is larger than expected, based upon the initial expansion speed and the time of flight.[13]

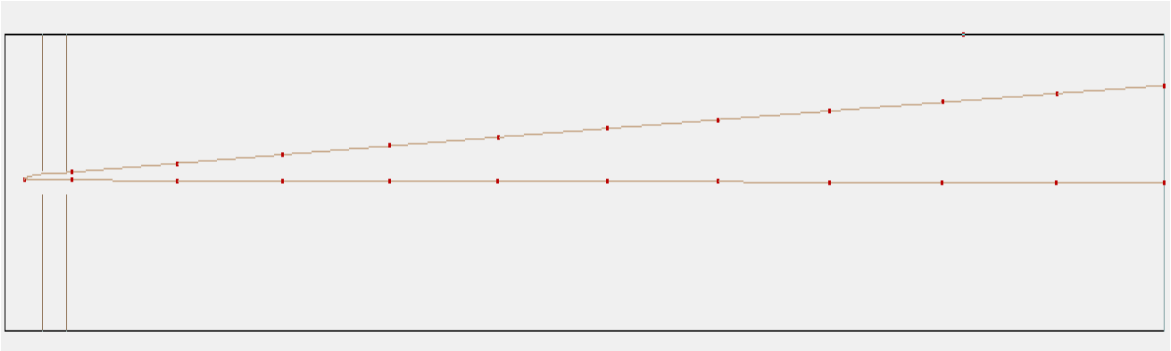

FIG. 14. The trajectories originate at y=0 mm with one ion ejected with a 90° elevation angle and other at 0 ° elevation angle.

The empirical relation between magnification factor N, expansion speed v, time of flight t and the radius R of the ring appearing on the image is described by

$$R = N\,v\,t \qquad (2.7)$$

Two ion trajectories originating at the same point with elevation angles of 0° and 90° were projected onto the detector, and the radius of the ring was obtained. With this parameter the magnification factor of the image was calculated to be 1.27. The radius of the image obtained for different voltages applied to the electrodes are given in Table 1.

TABLE 1. Results for the radius of the image and magnification factor based on different voltages applied to the electrodes, using ions with 15 amu mass and 1 eV of kinetic energy.

V_E (Volts)	V_R (Volts)	Radius of Image (mm)	Magnification Factor
500	275.37	58.33	1.27
750	413.06	41.51	1.27
1000	550.75	36.09	1.27
1250	688.43	32.33	1.28
1500	826.12	29.51	1.28

3.3 Monte-Carlo Image Creation

To simulate an image that is close to the image expected from experiments, a software program was written in Microsoft Visual Basic 6.0. An 8-bit 512×512 pixel image was obtained by simulating 1,000,000 trajectories with the extractor electrode voltage calculated from the SIMION simulation, kinetic energy of ions, amplitude of channels, magnification factor of the image and the anisotropy parameter as inputs.

The photofragments desorbed from the ice matrix will be ionized using the 2+1 REMPI process and the resulting photofragments are accelerated through the ion optics assembly before being projected on to the MCP.[27] The (*y, z*) coordinates of the photofragments at

the detector can be expressed as follows. This section is related to the back projection method published by Whitaker.[1]

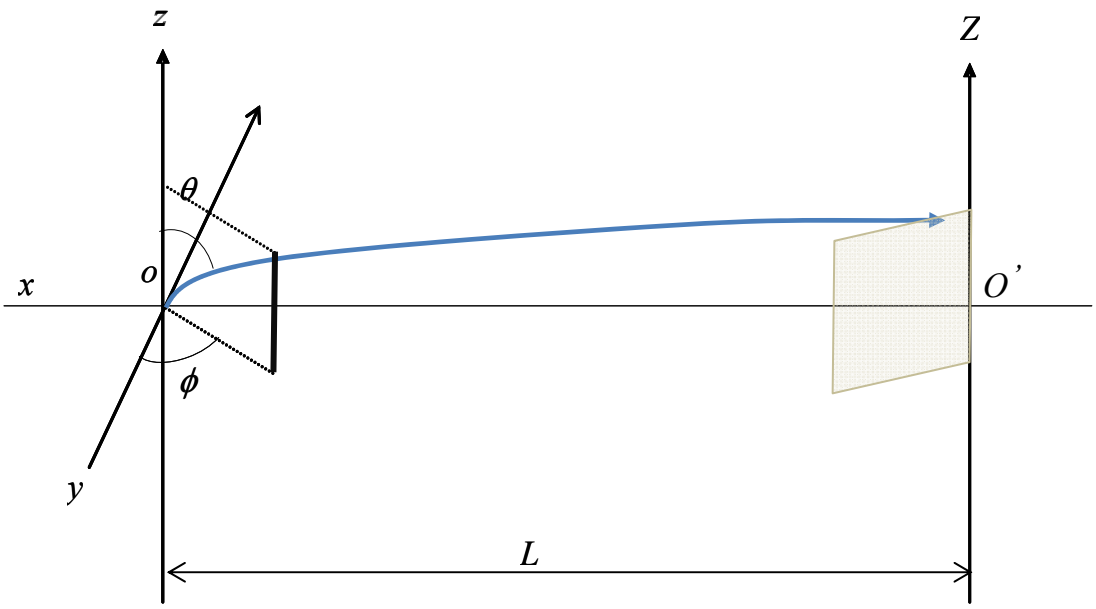

FIG.15. Schematic for the projection of ionized photoproducts (originating at point *O*) on to the detector.

As shown in Figure 15, the point of origin of the photofragments, which corresponds to the REMPI ionization region, is defined as origin ($x = y = z = 0$). The initial velocity distribution of the photofragments can be written using spherical polar coordinates θ, ϕ and the initial velocity v_0 as:

$$\begin{aligned} v_{ox} &= v_0 \sin\theta \cos\phi \\ v_{oy} &= v_0 \sin\theta \sin\phi \\ v_{oz} &= v_0 \cos\theta \end{aligned} \qquad (2.8)$$

The ionized fragments will then be accelerated through a homogenous electric field E, along the TOF axis O_x with a force of

$$F_x = Eq \tag{2.9}$$

where q is the elementary charge.

The co-ordinates (x, z) at the detector are calculated as

$$y = \frac{2L\cos\phi\sin\theta}{\rho}\left(\sqrt{\sin^2\phi\sin^2\theta+\rho} - \sin\phi\sin\theta\right) \tag{2.10}$$

$$z = \frac{2L\cos\theta}{\rho}\left(\sqrt{\sin^2\phi\sin^2\theta+\rho} - \sin\phi\sin\theta\right) \tag{2.11}$$

where ρ is the ratio between electrostatic energy acquired in the field and the initial kinetic energy in the particle

$$\rho = \frac{qEL}{\frac{1}{2}mv_o^2} \tag{2.12}$$

and L is the distance between the region where the desorbed products are ionized and detected.

Since the initial kinetic energy of the desorbed products are estimated to be less than 1 eV, and since the kinetic energy gained through the accelerating field is extremely large, the equations for positions (y, z) are reduced to:

$$y = \frac{2L\cos\phi\sin\theta}{\sqrt{\rho}} \tag{2.13}$$

$$z = \frac{2L\cos\theta}{\sqrt{\rho}} \tag{2.14}$$

The fragments from photodissociation are ejected parallel or perpendicular to the polarization direction of the light with an angular distribution given by

$$I(\theta) = \left(1 + \beta P_2(\cos\theta)\right) / 4\pi \tag{2.15}$$

where θ is the angle between the fragment velocity vector and light polarization direction, and $P_2(x) = (3x^2 - 1)/2$ is the second-order Legendre polynomial. The (*y*,*z*) co-ordinates are calculated by the Visual Basic program as stated below. The program generates three random numbers, R_1, R_2 and R_3, which are distributed evenly between zero and one. From R_3 one can calculate $\phi = 2\pi R_3$. However, θ is not calculated directly as $\theta = \pi R_2$ in the program, since even for an isotropic distribution this equation would bias towards intensity at the "poles" of the image. For an anisotropic distribution the intensity is given by equation (2.15).

Using a random number generator it is possible to construct random numbers taken from a variety of distributions. If there are equal distributions of random numbers R_1, R_2 and R_3 the random number generator can be used to generate the numbers. If the random numbers are of a linear distribution, they can be generated by the von Neumann algorithm. The von Neumann algorithm generates non-linearly distributed random numbers using a biased condition statement as follows.

This algorithm generates an even distribution of random numbers in the range ($x_{1,}$ x_3).

To generate a random number R uniformly on ($x_{1,}$ x_2) assuming we can generate randomly on the range ($x_{1,}$ x_3).

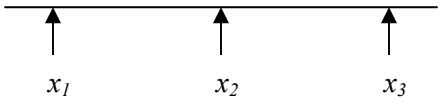

To generate a linearly distributed array of random numbers the algorithm is modified to

(a) Generate R_1 uniformly on (x_1, x_3) and generate R_2 uniformly on (x_1, x_3)

(b) If $R_1 < R_2$ then take R_1 as the random number on the distribution

(c) If not, go to (a).

The expression for θ is still more complicated and given in (2.15). We can then generate the random angular distribution in θ from:

(a) generate R_1 uniformly on (x_1, x_3) and generate R_2 uniformly on (x_1, x_3)

(b) if $(\beta_2 \times 0.5 \times (3 \times Cos(R_1 \times \pi)^2 - 1) + 1) < R_2$ then take R_1 as the random number on the distribution. The angle θ = arcos (R_2).

(c) if not, go to (a).

If the value obtained from the conditional statement is greater than R_2, then the value is kept without being discarded. The Visual Basic program therefore contained the following code:

If $(\beta_2 \times 0.5 \times (3 \times Cos(R_1 \times \pi)^2 - 1) + 1) / (1 - \beta_2 \times (-0.25 - Sgn(\beta_2 \times 0.75))) > R_2$

Then

$$\theta = \arccos(R_1)$$

$$\phi = 2\pi R_3$$

$$Y = \frac{2LCos(\phi)Sin\theta}{\sqrt{\rho}}$$

$$Z = \frac{2LCos(\theta)}{\sqrt{\rho}}$$

The expression $(1 - \beta_2 \times (-0.25 - Sgn(\beta_2 \times 0.75)))$ is a normalization factor for the anisotropy parameter. In Visual Basic the "*Sgn*" function returns an integer that indicates the sign of the operation. The Visual Basic code has been included in the appendix section.

The calculated co-ordinates of each ion are stored in an array. An image is calculated as counts of the number of events falling within each pixel. The code given below illustrates how binning into an image with a resolution of $res \times res$ pixels, can be used to increase the intensity of the pixels if two ions with the same co-ordinates are generated in a binned image. R_{max} is the maximum radius of the image.

$$Y_{image} = Int((Y / R_{max} + 1) * res / 2$$

$$Z_{image} = Int((Z / R_{max} + 1) * res / 2$$

$$IntImage(Y_{image}, Z_{image}) = IntImage(Y_{image}, Z_{image}) + 1$$

To verify that the simulation code actually works, the 3D simulated image was then inverted with the onion-peeling program[20] to obtain a 2D slice through the center of the image. The 2D image provides information about velocity profiles and spatial anisotropy parameters and is expected to recover the input parameters from the simulation.

The program calculates angular distribution at a given radius. The angular distributions resulting from an ionization process can be expressed as a sum over Legendre polynomial components:

$$I(\theta) = c\sum_{n=0}^{N} \beta_n P_n(\cos\theta) \qquad (2.16)$$

Where N depends on the number of photons driving the process, and θ is the angle between the axis of polarization of the photolysis light and the velocity of the fragments. If the normalization coefficient c is chosen so that $\beta_0 = 1$, the remaining coefficients β_n are known as the spatial anisotropy parameters.[20]

The onion-peeling program transforms the image from Cartesian coordinates to polar coordinates[28-30], and by fitting the angular distribution to the above function and the anisotropy parameter , β_2 is determined for each radius.

The values for the spatial anisotropy parameters that were used to construct the simulation and those recovered from the onion-peeling program and the Abel transform were then

compared. A discrepancy between the simulation input and the output were observed because the velocity distributions are set very narrow during the inversion process and that throws off the program. Therefore the simulation was repeated with velocity broadened distributions and the spatial anisotropy parameters were recovered. The results are given in Table 2 while the inverted images are given in Figure 16.

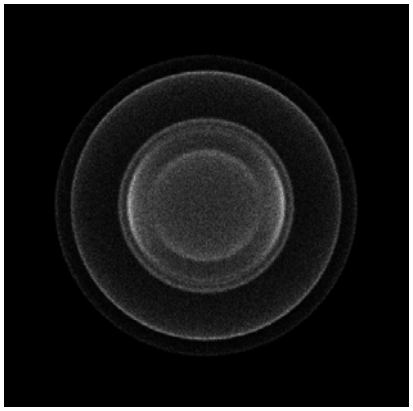

Simulated Image from the
Visual Basic Program

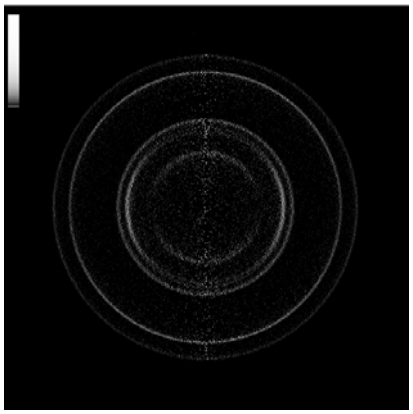

Inverted Image from the
Onion Peeling Program

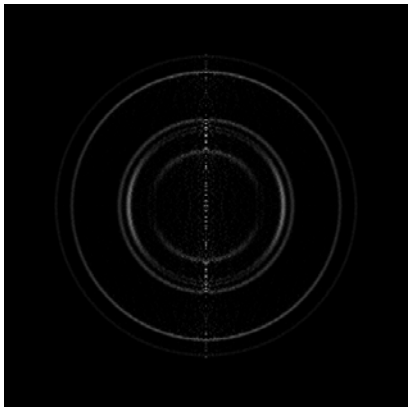

Inverted Image from the Abel
transform

FIG.16. Typical image simulated by the Visual Basic program (top) using broadened velocity distributions, the Inverted image from the Onion Peeling Program (middle), and the Inverted image from the Abel Transform (bottom).

TABLE 2. Anisotropy parameters for simulated image and inverted image from the velocity broadened distribution.

β_2 used for the simulation	β_2 recovered from the Onion Peeling Program	β_2 recovered from the Abel transform
1.8	1.77	1.82
-1	-1.03	-0.94
0	0.08	0.1
0.5	0.5	0.5
-0.5	-0.51	-0.52

3.4 Conclusion

A significant amount of information about the ice matrix and the desorbed species from the ice surface can be extracted by combining the REMPI spectroscopy and FT-IR spectroscopy. In this section, the principle of the velocity map imaging spectrometer has been discussed, together with the inversion procedure to extract physical information from the acquired images. Resolution characteristics of the velocity map imaging spectrometer have been investigated with the ion trajectories simulation using Simion 7.0 software package. The results from this simulation provided an understanding of the voltages that can be applied to the ion optics assembly to optimize the resolution of the

experimental image of photoproducts. With the Visual Basic program discussed in this section, it is possible to simulate the images of the desorbed species from the ice surface. However, the expected image would be a semi-circle, as desorbed species are only directed to the space above the cold tip. These simulations will aid in acquiring the velocity profile of the photoproducts, and provide more accurate energy distributions to propose mechanisms for reactions in water ice and its constituents.

References for Chapter 3

[1]B. J. Whitaker, Imaging in Molecular Dynamics (Cambridge University Press, Cambridge, 2003).

[2]B. J. Whitaker, Image Reconstruction: The Abel Transform, in: A. G. Suits, R. E. Continetti (Eds.), ACS Symposium Series, Vol. 68, Oxford University Press, 2000.

[3]A. Heck, Europ. Mass. Sectr. **3**, 171 (1997).

[4]P. L. Houston, Acc. Chem. Res. **28**, 458 (1995).

[5]P. L. Houston, J. Phys. Chem. **100**, 12757 (1996).

[6]S. H. Lee, H. I. Lee, and Y. T. Lee, J. Chem. Phys. **121**, 11053 (2004).

[7]J. Solomon, J. Chem. Phys. **47**, 889 (1967).

[8]D. W. Chandler, and P. L. Houstan, J. Chem. Phys. **87**, 1445 (1987).

[9]W. C. Wiley, I. H. McLaren, Rev. Sci. Instrum. **26**, 1150 (1955).

[10]A. J. R. Heck, and D. W. Chandler, Annu. Rev. Phys. Chem. **46**, 335 (1995).

[11]C. Vallance, Philos. Trans. R. Soc. London, A, **362**, 2591 (2004).

[12]D. M. Sonnefroh, and K. Liu, Chem. Phys. Lett. **176**, 183 (1991).

[13]A. T. J. B. Eppink, and D. H. Parker, Rev. Sci. Instrum. **68**, 9 (1997).

[14]B. Y. Chang, R. C. Hoetzlein, J. A. Mueller, J. D. Geiser, and P. L. Houston, Rev. Sci. Instrum. **69**, 1665 (1998).

[15]A. S. Bracker, E. R. Wouters, A. G. Suits, and O. S. Vasyutinskii, J. Chem. Phys. **110**, 14 (1999).

[16]G. A. Gracia, L. Nahon, and I. Powis, Rev. Sci. Instrum. **75**, 4989 (2004).

[17]C. Bordas, F. Pauling, H. Helm, and D. L. Huestis, Rev. Sci. Instrum. **67**, 6 (1996).

[18]M. J. Bass, M. Brouard, A. P. Clark, and C. Vallence, J. Chem. Phys. **117**, 19 (2002).

[19]M. J. Bass, M. Brouard, A. P. Clark, B. Martinez-Haya, and C. Vallence, Phys. Chem. Chem. Phys. **5**, 856 (2003).

[20]S. Manzhos and H.-P. Loock, Comp. Phys. Commun.,**154**, 76(2003).

[21]R. H. Brown and D. P. Cruikshank, Annu. Rev. Earth Planet Sci. **25**, 243 (1997).

[22]J. E. Schaff and J. T. Roberts, J. Phys. Chem. **100**, 14151 (1996).

[23]A. Susa and S. Koda, Meas. Sci. Technol. **15**, 1230 (2004).

[24]S. Malyk, G. Kumi, H. Reisler, and C. Witting, J. Phys. Chem. **111**, 13365 (2007).

[25]D. L. Cocke, J. A. G. Gomes, J. L. Gossage, K. Li, C.-J. Lin, S. Tandel, App. Spec. **58**, 528 (2004).

[26]D. A. Dahl, J. E. Delmore, and A. D. Appelhans, Rev. Sci. Instrum. **61**, 607 (1990).

[27]C. Romanescu, S. Manzhos, D. Boldovsky, J. Clarke, H.-P. Loock, J. Chem. Phys., **120**, 767 (2004).

[28]J. Winterhalter, D. Maier, J. Honerkamp, V. Schyja, and H. Helm, H. J. Chem. Phys., **110**, 11187 (1999).

[29]V. Dribinski, A. Ossadtchi, V. A. Mandelshtam, and H. Reisler, Rev. Sci. Instrum. **73**, 2634 (2002).

[30]O. Ghafur, W. Siu, P. Johnson, M. F. Kling, M. Drescher, and M. J. J. Vrakking, Rev. Sci. Instrum. **80**, 033110 (2009).

Chapter 4
Programming of Instrumental Components in the Experiment

4.0 Programming with LabVIEW

Laboratory Virtual Instrumentation Engineering Workbench (LabVIEW) is a powerful tool developed by National Instruments (NI) that enables computerized control of instruments. The building blocks used in LabVIEW programming are known as Virtual Instruments (VIs). The programming approach in VIs is the utilization of graphical programming code, which makes use of graphs, charts, gauges, and meters that are created to emulate an instrument.[1] With this programming approach LabVIEW has introduced a user-friendly visual programming technique that allows the controlling of experimental conditions, remote operation of instruments, and analysis of data. In comparison to traditional instruments, the VIs created in LabVIEW provide more user-defined and more application-oriented solutions.[1] This chapter illustrates the programming of the instrumental components of the experiment using LabVIEW 8.6.

The graphical development environment in LabVIEW has two main components, which are the front panel and the block diagram. The front panel is the User Interface (UI), which is the visual representation of the application. It is typically characterized by the knobs, buttons, and controls which emulate the traditional instrument.[1] The inputs to the application are provided, and the outputs are displayed using the front panel. The

block diagram contains the graphical source code and reflects a flow chart rather than the usual lines of code seen in computer programs. LabVIEW supports modularity and breaks down tasks to manageable sub-tasks, such as nodes and sub-VIs. Nodes in LabVIEW represent functions, operators, and subroutines in standard programming languages.[1] Structures are type of nodes that are commonly used in LabVIEW to execute code repeatedly or conditionally. They are comparable to the loops, conditional statements, and case structures used in text-based programming. These nodes and sub-VIs can also make use of the libraries available for the instrument. Terminals in the block diagram serve as entry and exit points for data between the front panel and the block diagram. The terminals, nodes, and sub-VIs are connected to each other to perform a task, using virtual wire connections. Wires serve as data paths between source and destination terminals. They are comparable to variables in text-based programming languages.[1] In text-based programming languages, different data types are used to eliminate the confusion of variables. LabVIEW implements the same principle in graphical programming by using different colors and styles in its wiring.[1] Hence, the block diagram is a visual representation of the inputs, functions, sub-VIs, wired connections, and outputs. The functionality of a LabVIEW program in comparison to a text-based program is illustrated in the following example. Let us suppose that a user would like to specify the number of measurements he wants from a certain device, and would like to see how many measurements the device has taken while he is running the experiment. This repetitive cycle of measurements can be implemented using a “for loop” in a standard

programming language. The text based code written for this loop using Visual Basic will be as follows:

```
Dim NumberOfSamples, i As Integer
  For i = 1 To NumberOfSamples
    Print "Display Number", i
  Next i
```

The same loop written using the graphical code in LabVIEW will be as shown in Figure 17.

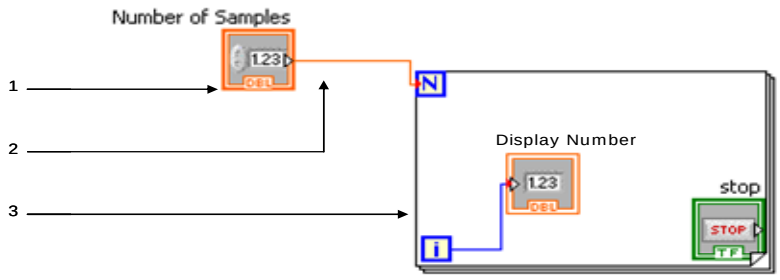

Block Diagram Icons:

1- Numeric Control Terminal

2- Wire Data Path

3- For Loop

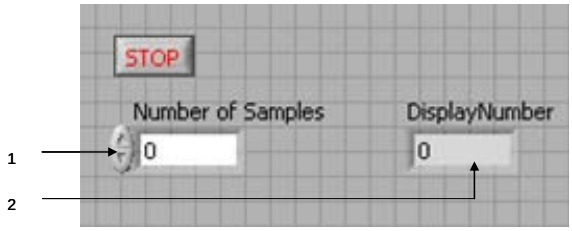

Front Panel Icons:

1- Digital Control

2- Digital Indicator

FIG.17. Implementation of a “for loop” in LabVIEW- Block Diagram and Front Panel.

The principle followed in the source code of the LabVIEW program is similar to the text-based programming languages. However, LabVIEW is advantageous in terms of not having to declare or initialize variables as opposed to most programming languages. An additional advantage is that LabVIEW simultaneously creates the front panel as the programming on the block diagram takes places.[1]

LabVIEW also allows the utilization of built-in tools such as Measurements Automation Explorer for programming the Data Acquisition Devices (DAQ). The standard I/O language for instrumentation programming is Virtual Instrumentation Software Architecture (VISA). VISA is a capable of controlling General Purpose Interface Bus (GPIB) and serial instruments, and call lower level drivers.[1] VISA resources, operations, and attributes commonly used in LabVIEW programming. The VI communicates with a device by establishing a VISA session. The basics of this process are used in LabVIEW programming as shown in Figure 18.

FIG.18. Communicating with an instrument.

The instrument I/O tools in LabVIEW create the components required to communicate with an external device attached to a serial or a GPIB port and provides the ability to switch between interfaces.

This chapter discusses the programming of the instruments used in the experiment by using LabVIEW 8.6. The experimental details of velocity map imaging have been discussed in detail in chapter 3. An overview of the experimental section will be presented in the following section in light of the programming process.

The main elements of the programming environment are a pulsed laser system, a Molecular Beam Valve (MBV), and a charged particle detection system. The pulsed laser system is comprised of a photolysis laser (Lambda Physik, LPX200, Excimer Laser) and a probe laser (Scanmate, Lambda Physik, Dye Laser) pumped by a Nd:YAG Laser (Continuum). The timing of the photolysis and probe lasers is achieved through a delay generator (DG 535, Stanford Research Systems) and a PCI6602 timing board via the *DG535 VI* and the *PCI6602 VI*. The latter is used to control the MBV as well. The ions generated in the vacuum chamber are accelerated through an ion optics assembly and pass through a time-of-flight (TOF) region before hitting the MCP. The high voltage applied to the ion optics assembly and the MCP (Chevron configuration, Burle Electro-Optics, Inc) is controlled by the *PS350 High Voltage Power Supply VI*. The MCP is gated with a high voltage pulse to allow only ions of interest to be detected. The TOF profile of these ions is observed through a digital oscilloscope (Tektronix, DPO3034 series) and

recorded as a function of the probe laser wavelength via the *Stepper Motor Scope REMPI VI.* The cascade of electrons that strike the phosphor screen creates an ion image which is recorded by a CCD camera (Sensicam, Optikon, 12 bit, 1280 x 1024 resolution) controlled by the *Imaging VI*. Figure 19 shows the layout of the VIs for data acquisition.

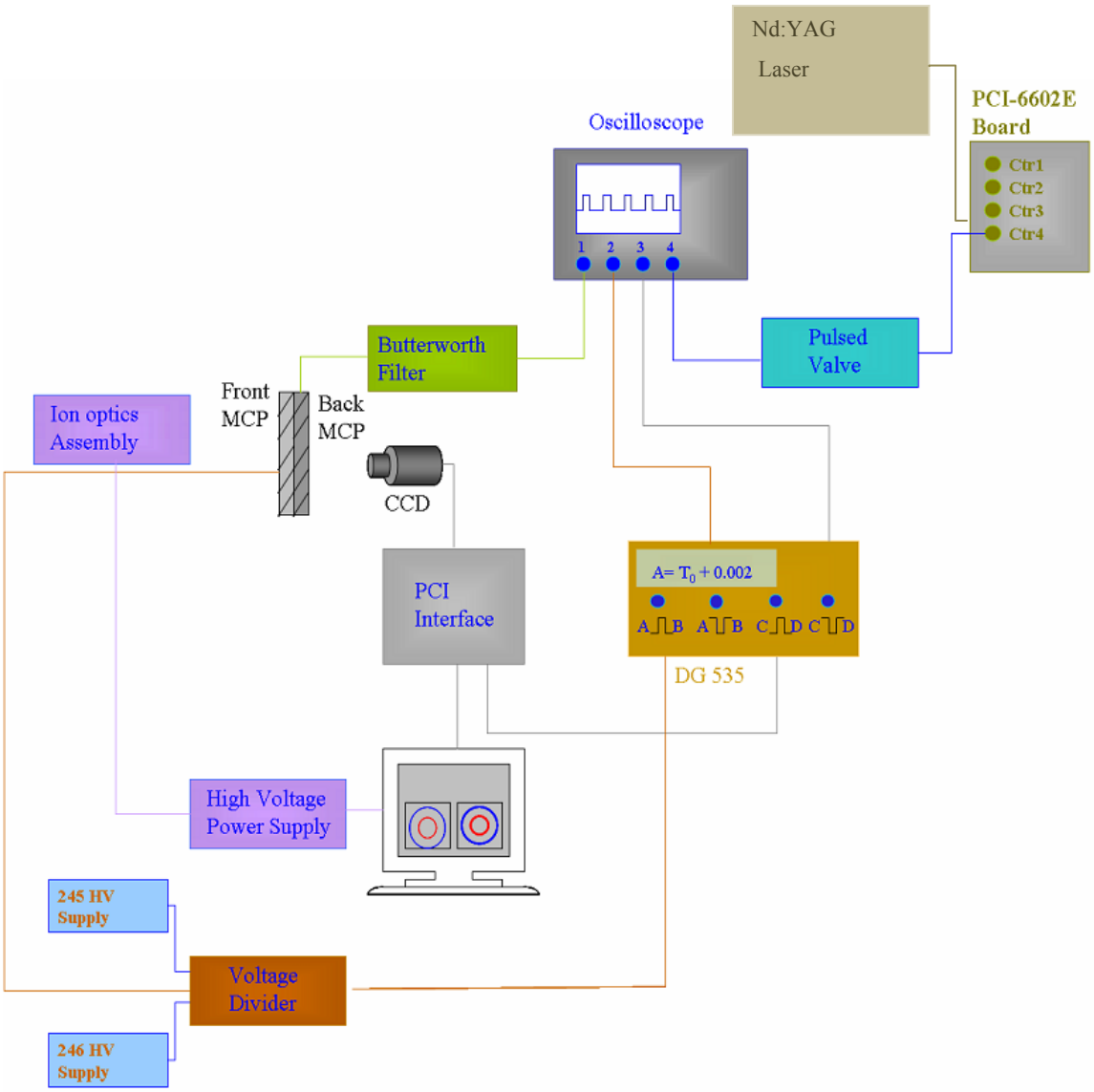

Fig.19. Schematic for the data acquisition system using *VI*s.

4.1 PS 350 series High Voltage Power Supply

The four PS 350 series High Voltage Power Supplies are used to control the voltages applied to the repeller plate, back MCP, extractor plate, and the phosphor screen. The PS 350 series High Voltage Power Supply is remotely manipulated by the Lab VIEW program via the GPIB interface. In order to communicate with the GPIB interface, the address of the PS 350 device must be configured. This is achieved by selecting the appropriate GPIB name from the VISA resource drop-down menu. The VISA resource name is unique to an instrument I/O session. It specifies which device to communicate with and all the configuration information to perform the I/O. This prompts the opening of a session with the selected device specified by the VISA resource name and the program returns a session identifier that can be used to call any other operations in the power supply. This process is shown in Figure 2.

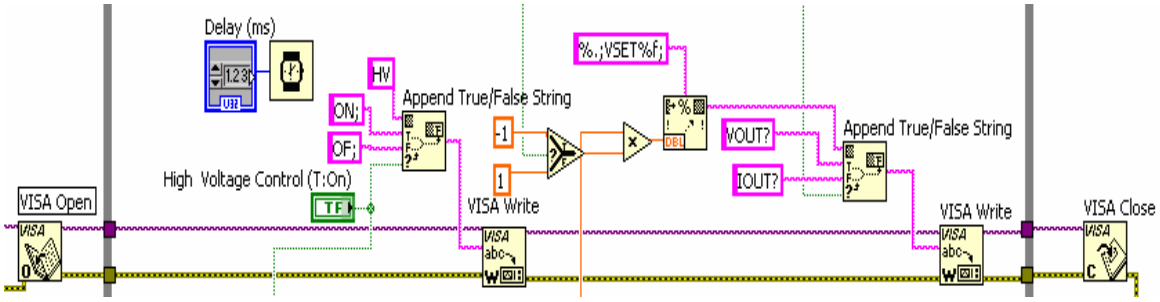

FIG.20. Communication with the device.

The front panel in Figure 21 allows the user to specify the exact voltages required using the "start" and "end" controls. The ability to change the voltage in small increments is important to prevent damage to the assembly, and also to observe the changes in the image when the repeller and extractor voltages are adjusted. The "step" and "increase/decrease" controls allow this manipulation. The output voltage is displayed in the "VCurrent" box. The output voltage cannot be set higher than the voltage limit.[1]

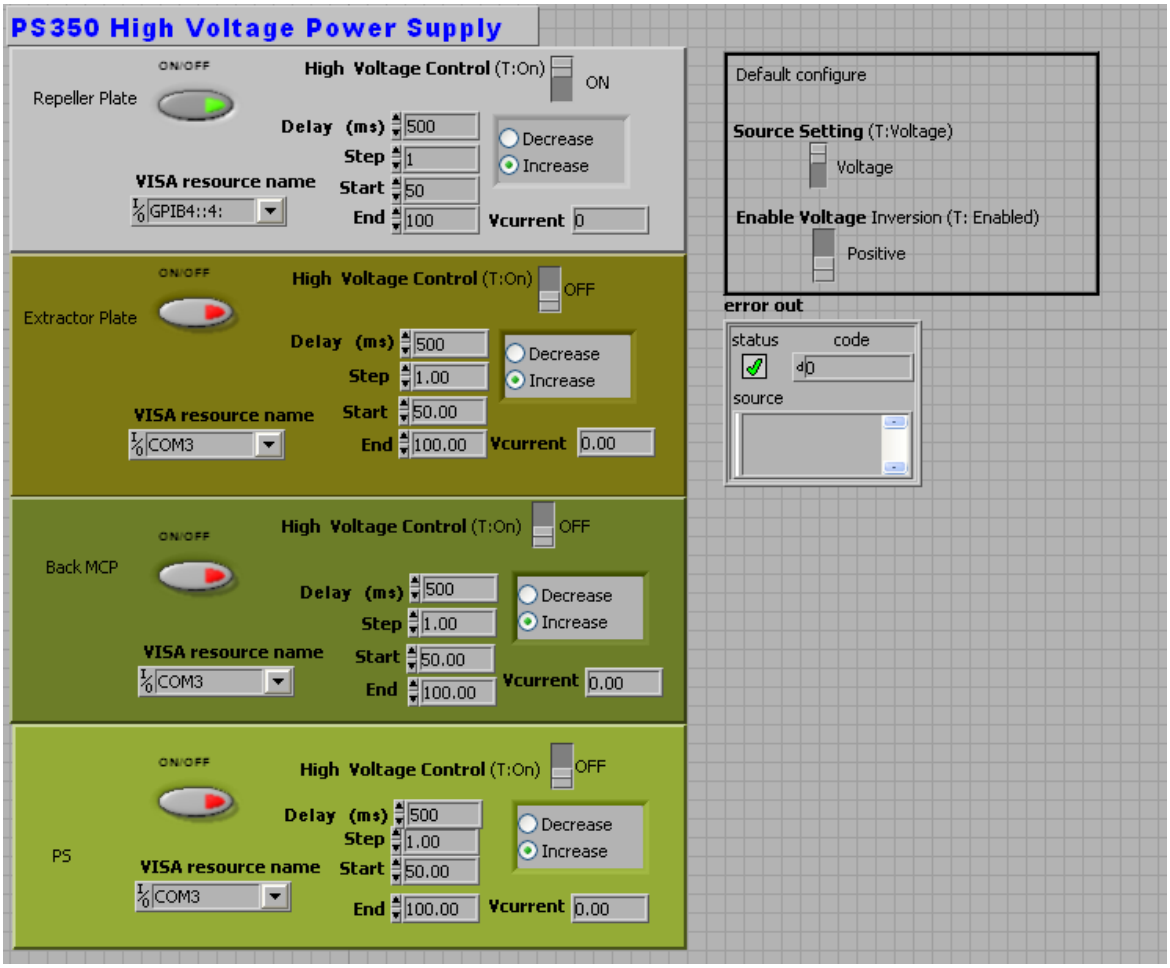

FIG.21. Front panel of power supply.

In addition, if the output exceeds 10% of the full scale, the unit trips and the high voltage is disabled. If this occurs, a 'VTRP' (voltage trip) message appears in the panel. The "Source Setting" sliding switch allows the user to specify the source before setting up its limit. The default has been set to voltage and the switch manipulates the voltage setting, provided that the front panel switch is turned on the instrument. If the switch is in the OFF position while trying to set the high voltage, the high voltage is left off and an execution error is reported. The "Enable Voltage Inversion" control changes the voltage from positive to negative. All of the above-mentioned inputs are directed to the VISA Write Function in LabVIEW and the data is then written into the device.

4.2 DG 535 Digital Delay and Pulse Generator

The DG 535 can produce four digitally controlled time intervals. These time intervals can be controlled by using a LabVIEW program through the GPIB connector. The IEEE-488.2 connector allows the computer to control the DG 535. The DG 535 consists of five delay out BNCs named T_0, A, B, C, and D.[5] T_0 sets the start time for the timing interval when the DG 535 receives a pulse from the master trigger. The LabVIEW program allows the manipulation of the delays in the channels A, B, C, and D. The delay outputs A, B, C, and D can then be set with respect to T_0 or each other from 0 to 1000 s with increments of 5 ps.[5] For example, the delay menu can be set as:

$A = T_0 + 4$ ns

$B = A + 5$ ns

$C = T_0 + 2$ μs

$D = C + 0$

where channel A is referenced to T_0 and channel B is set to A's delay plus 5 ns. This allows the program to specify the start time and the pulse width. The program allows the user to control the each channel through the "Time Base Menu" in the front panel and the "Delay Menu."

The DG 535 can be triggered internally or externally. The external trigger port on the DG 535 is connected to the Excimer laser (Lambda Physik LPX 200i). The four pulse outputs are labeled A∪B, A∩B, C∪D, and C∩D. The pulse output A∩B is connected to the high voltage gate and A∪B displays the same pulse on the oscilloscope. The pulse output C∪D is connected to the "Trig-in" port for the CCD camera on the computer, in order to control the CCD exposure time and C∩D displays the same pulse on the oscilloscope. The front panel of the DG535 VI is shown in Figure 22.

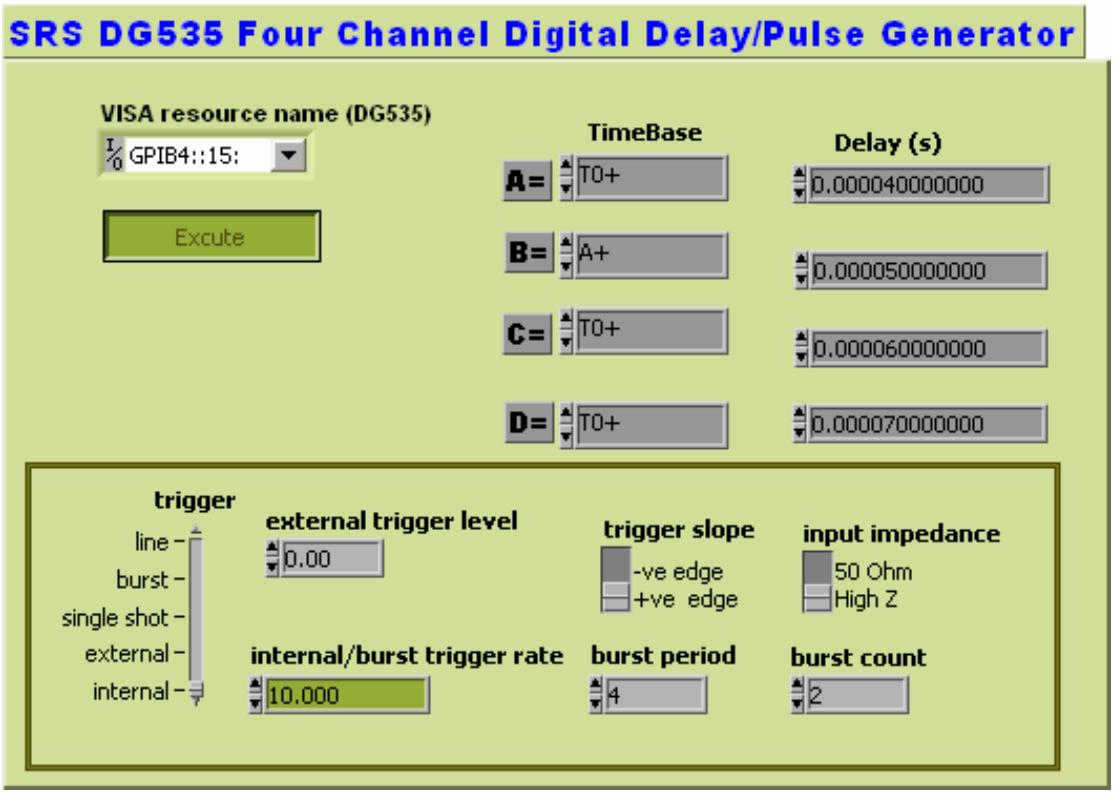

FIG.22. DG 535 front panel.

The front panel allows the internal trigger mode to be manipulated by setting the trigger rate; the external trigger mode can be controlled by specifying the threshold trigger level, slope and termination impedance of the external trigger input. The burst mode can be controlled by specifying the trigger rate, the burst period, and number of pulses per burst.

4.3 Data Acquisition with LabVIEW

The primary Data Acquisition (DAQ) processes used in this section generate signals, analysis, and presentations on the computer.[2] This process is implemented by utilizing the main components of DAQ which are data signals, DAQ hardware and driver applications.[2] Using these components, it is possible to use counters and timers to generate pulses and pulse trains with LabVIEW. Virtual channels for data acquisition, triggering and synchronization can be created with LabVIEW palettes and Sub-VIs.

4.3.1 Triggering

The triggering of events in data acquisition can occur in three possible ways:[1]

1. External triggering
2. Internal triggering
3. Software-generated triggering

External triggering occurs when an interface uses digital pulses from specialized hardware or equipment to synchronize events. Internal triggering is common in DAQ devices and occurs when an inbuilt-comparator detects the signal crossing of a specified signal level and in turn triggers an event.[1] In software-generated triggering, a software program is responsible for the occurrence of event such as data acquisition.

In this section, a LabVIEW program is used for data acquisition through NI-PCI 6602E card which is plugged into a computer through a connector block (CB-68LP). NI-PCI

counter / timer devices can be easily used across multiple hardware devices as they are equipped with a Real Time System Integration (RTSI) bus line.[1]

4.3.2 Triggering with PCI 6602E VI

This VI has been written using the DAQ features in order to synchronize instrument components in the experiment such as the Nd : YAG laser, Delay Generator, and Pulsed Valve. The synchronization process is performed by the "Master Device" and "Slave Device" panels seen in the front panel of the VI. Hardware synchronization is achieved through the RTSI cable, which is a high-speed digital bus that exchanges timing signals between NI boards. In the LabVIEW programming environment, the NI-DAQ driver is responsible for routing and driving the RTSI bus automatically via the *Route Signal VI*. The LabVIEW program written for the PCI-6602 makes use of this feature by generating a pulse in counter 0 and then translating that pulse to all the counters through the RTSI bus, thereby synchronizing the connected devices.[2,6]

The pulse for the master device was programmed by using the classes of the DAQ Create Virtual Channel. The numerous classes of the DAQ Create Virtual Channel are able to perform functions such as temperature measurement, voltage generation, event counting, and corresponding with I/O channels.[1] The instance of this channel employed in programming PCI 6602 is "CO Pulse Time." The CO Pulse Time Channel creates a digital pulse defined by the pulse width and initial delay specified by the user. The initial

state of the pulse was defined as "low."[3] The basic implementation of DAQ features to generate a pulse is shown in Figure 23.

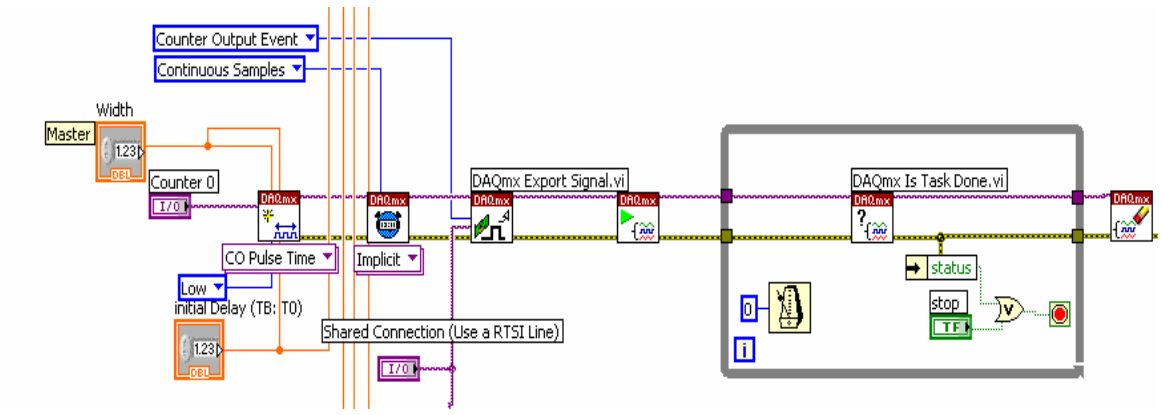

FIG.23. DAQ in the *PCI 6602E VI.*

4.3.2.1 Implementation of the PCI 6602E VI

The input "task in" is then provided to the *Timing Implicit VI*, which in turn, configures the duration of the pulse generation and the number of pulses to generate.[2] The *Export Signal VI* then routes the control signal to the terminal specified by the user.[3] The *Start VI* initiates pulse generation, and the *Is Task Done VI* queries the status of the task and indicates the completion of the execution cycle.[3] Once the execution cycle has been

completed, the *Clear Task VI* stops the task, releases the resources reserved, and clears the task.[3]

Similarly, the digital pulses for all the slave devices are generated by the CO Pulse Time Channel. The I/O counter denotes the names of the counters to create the virtual channels. The DAQmx physical channel constant provides all the counters and devices installed in the system, and they can be selected from the drop-down menu in the front panel.[3]

4.3.2.2 Front Panel of the PCI 6602E VI

The front panel is comprised of two main panels for master and slave devices as shown in Figure 24. In the master device panel, the user is able to input the amount of time the pulse must be high, and the amount of time (in seconds) to wait before generating the first pulse by using the digital controls for "width" and "initial delay", respectively. The initial delay in the master device is defined as T_0.

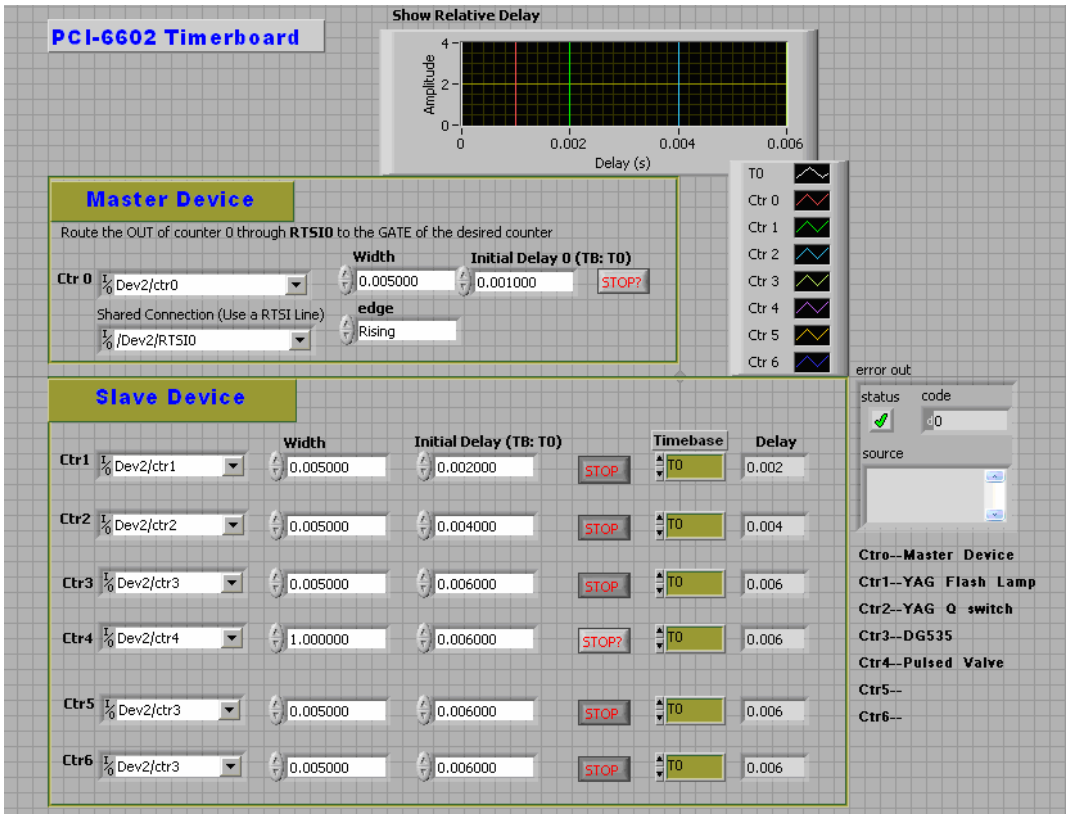

FIG.24. Front Panel of *PCI 6602 VI.*

In the slave device panel, the counters 1-4 have been assigned to the following devices:

Counter 1 – Nd: YAG laser flash lamp

Counter 2 – Nd: YAG laser Q switch

Counter 3 – DG 535

Counter 4 – Pulsed Valve

The names of the counters for each of the devices can be selected from the DAQ-physical-channel-constants drop-down menu. The user is also able to specify the pulse width and initial delay for each counter using the respective digital controls. The time base indicator displays the reference for the delay in each counter. The default setting for the time base indicator in all the counters has been set to T_0. However, the user is able to change this reference using the time base digital indicator. The delay indicator displays the calculated total delay for each counter based on the initial delay and time base. The delay is set with reference to the rising edge from the pulse in counter 0. Total delay for each counter is displayed in the "Show Relative Delay" wave graph. Any errors that occur during operation will be displayed in the "Error out" panel.

4.4 Collecting TOF and REMPI spectra using LabVIEW

The following section discusses details of the VI written to collect TOF and REMPI spectra. The TOF spectra were collected using an oscilloscope and were transferred to the computer for analysis. The REMPI spectrum for each species is then calculated from the TOF spectrum. Since the TOF profiles are recorded as a function of the probe laser wavelength, a stepper motor unit was utilized to manipulate the probe laser wavelength using the computer. Hence, the VI described in this section has three panels:

1. Stepper motor panel to control probe laser

2. Oscilloscope panel to store TOF spectra

3. TOF and REMPI spectra panels

Each of these components will be discussed in the following section.

4.4.1 Stepper motor panel to control probe laser

The ability to control the probe laser wavelength is important in aligning the probe laser and when collecting the TOF spectrum. This is achieved through a stepper motor (NEMA 17 Unipolar) that controls the grating of the laser. The stepper motor, in turn, is controlled via a data acquisition device (Measurements Computing, USB1208FS) that triggers the stepper motor driver (QK179). These devices are shown in Figure 25.

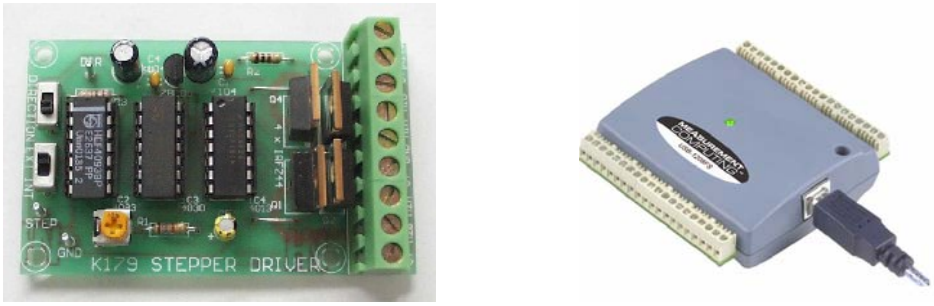

FIG.25. Stepper motor controller and data acquisition device.

4.4.1.1 Implementation of the stepper motor controller

The address of the driver port and the direction of rotation in the stepper motor have been configured using VIs for the data acquisition device from Measurements Computing, as given in Figure 11. These VIs allow the port to be configured as an output port and to set the direction bit. The stepper motor program can be used from a stand-alone VI to align the probe laser or from the QK179 panel on the *Stepper Motor Scope REMPI VI* to collect TOF spectra.

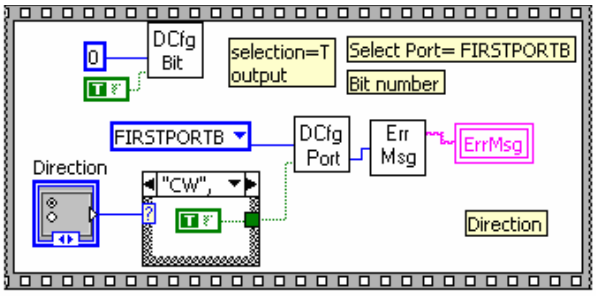

FIG.26. Block diagram to change direction of rotation in the stepper motor.

4.4.1.2 Front panel of the stepper motor controller

The front panel of the sub VI is given in Figure 27. In it the user can specify the direction of rotation for the motor and the start wavelength. The default settings for the pulse width have been set to 5, the delay has been set to 0, and the number of steps per

loop has been set to 200. Upon execution, the current wavelength of the probe laser will be indicated in the panel.

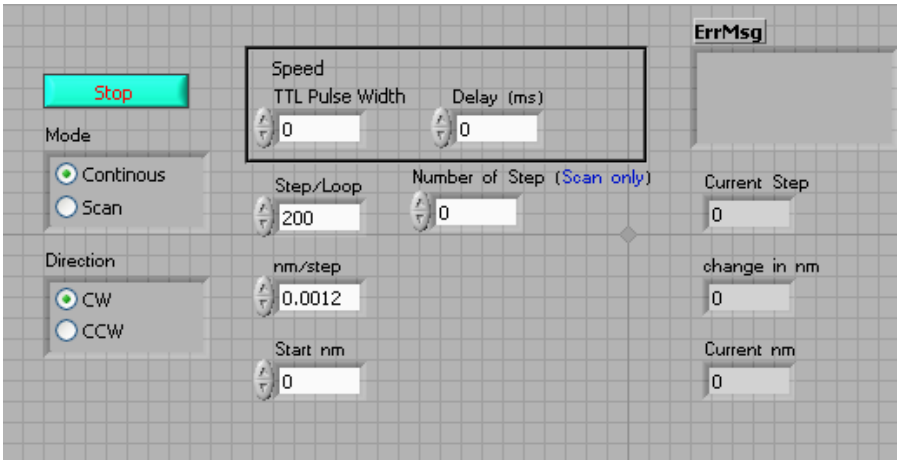

FIG.27. Front Panel of the *Stepper motor sub VI.*

4.4.2 Oscilloscope panel to store TOF spectra

4.4.1.3 Front panel of the oscilloscope

The TOF spectrum is observed in the digital phosphor oscilloscope as shown in Figure 28. The "Remote Control" button starts the execution of the DPO3034 panel. The VISA resource name of the oscilloscope can be selected from the drop-down menu. By specifying the VISA resource name, the user allows the computer to acquire data from the oscilloscope through the USB cable.[7] The digital control for channels allows the user to display the waveform in the desired channel. The "Maximum Time" control specifies

the amount of time to wait for the acquisition of data. The default is set to 10000 ms. The "Save" button saves the spectrum into the path specified by the user.

4.4.1.4 Implementation of the oscilloscope

The DPO3034 panel has been programmed with the following sequence of operations: Initializing the session with the instrument; sequentially acquiring data; waiting until the operation is complete; acquiring the waveform; and closing the session.[7] The *Single Waveform VI* initiates acquisition based on the configuration information, waits for the acquisition to complete, and returns the requested waveform. The *Close VI* runs an instrument error query before closing the session.[3,10]

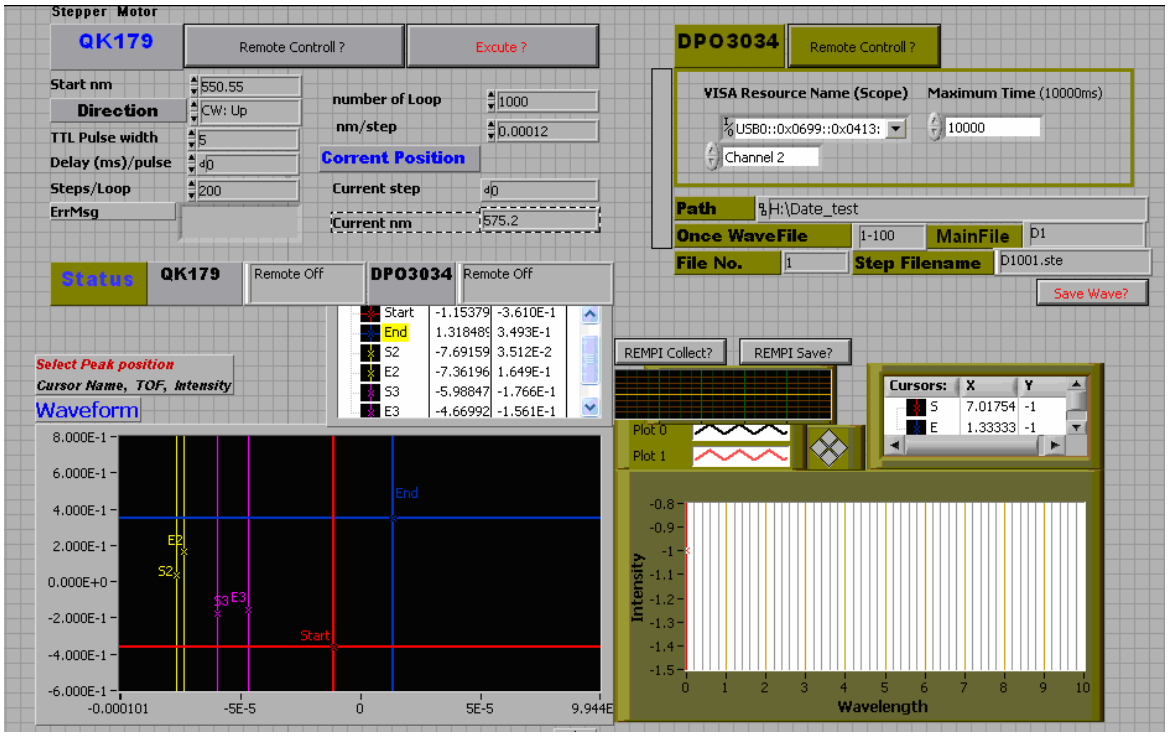

FIG.28. Front panel of the *Stepper Motor Scope REMPI VI.*

4.4.3 TOF and REMPI spectra panels

When the voltage applied to the MCP exceeds 1500 V, the MCP turns into the gain mode and can be used to gate ions of interest.[8,9] The TOF profiles are used to record ions as a function of wavelength of the probe laser. The TOF spectrum is then exported from the oscilloscope to the computer using the *DPO3034 sub-VI* and is displayed in the "Waveform" graph on the front panel in the *Stepper Motor Scope REMPI VI*. The waveform graph has a pair of horizontal cursors and four vertical cursor units. Each vertical cursor unit is comprised of a start and end cursor. In order to form the REMPI spectrum, the user must select the desired peak for analysis by positioning the cursors. The execution of this program can be initialized by the "REMPI Collect" button. The REMPI spectrum is produced by calculating the area of the TOF peaks of interest as a function of wavelength. The REMPI spectrum will then be displayed in the "REMPI Waveform" panel, and the spectrum can be saved to a user-specified location with the "REMPI save" button.

4.5 Imaging VI

The SensiCam system consists of two major components, which are the PCI interface board and the camera head.[11] LabVIEW communicates with the PCI interface board by using the SENNTPCI.DLL libraries. The PCI board communicates with the camera through a high-speed serial link. Camera control is performed by sending the

Camera Operation Code (COC) to the camera head.[12] Once the COC is uploaded to the camera head, exposure commences. COC will specify the parameters required to create an exposure. These parameters include trigger mode, delay from trigger to start exposure, region of interest, and binning. These parameters are included in the front panel of the Imaging VI.[12] The procedure used in this VI is as follows:

- Initialize the camera
- Upload the COC
- Start the exposure
- Wait until exposure terminates
- Retrieve imaging data

The front panel allows the user to specify the board number, run mode, mode of operation, and the read out mode. The board number inputs the board ID to the VI, the run mode controls single or continuous trigger exposure, the mode of operation initializes the code, and the read out mode specifies if the read out is upright or inverted. The CCD temperature should be approximately -13˚C and the temperature of the electronics should be maintained at 33˚C. These temperatures are displayed on the respective thermometers on the front panel.

The camera controls panel allows the user to specify the programmable controls. The "Camera Type" digital control allows the user to select the model of the camera connected. The choice of the camera model determines the behavior of the other

parameters. “Horizontal binning” combines pixels horizontally and “Vertical binning” combines pixels vertically for increased sensitivity. The four digital controls of ROI Left, ROI Right, ROI Top, and ROI Bottom specify the region of interest.

The camera information panel displays the specifications such as resolution, camera ID, CCD type, and temperature control. The image size status is used to display error codes along with the error out panel. The horizontal and vertical size indicators display the number of pixels in the image. The “image grab” can be used to save data to a user specified location.

The “Image 12 bit” panel shows each image shot at any given time, the “Count 12 bit” panel shows the sum of several shots, and the “Image 16 bit” panel scales the 0-4096 grayscale values of the 12 bit images up to 0-65535 and displays it as a 16 bit file. The front panel for the Imaging VI is given in Figures 29 and 30.

4.5.1 Implementation of the *Imaging VI*

The *Imaging VI* has been programmed using several sub VIs made for SensiCam.[12] For example, the *SCSetBoard VI* controls the communication with the board, *SCSetMode VI* sets the mode of operation for subsequent camera function calls, the *SCGetStatus VI* interrogates the camera for configuration and temperature information, and the *SCGetImageSize VI* determines the number of horizontal and vertical pixels in the current

image configuration. The scaling of the 12 bit image to a 16 bit image and normalizing it, has been implemented using a two dimensional array. Part of the block diagram is shown in Figure 31.

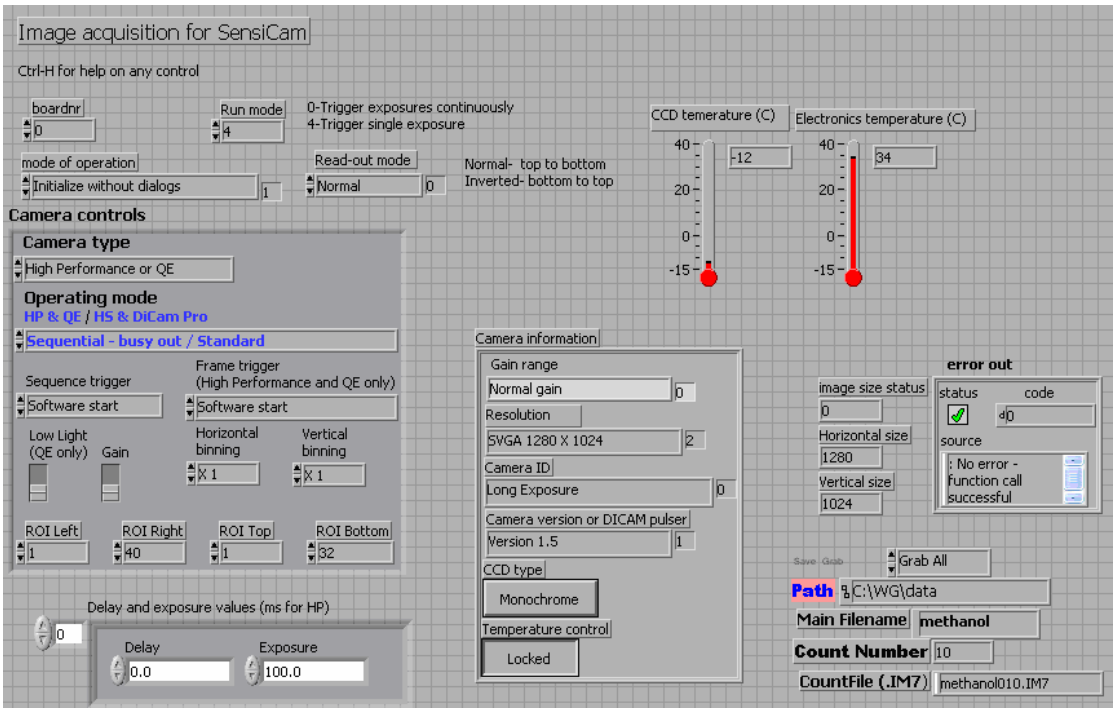

FIG.29. *Imaging VI*, front panel 1 for user inputs.

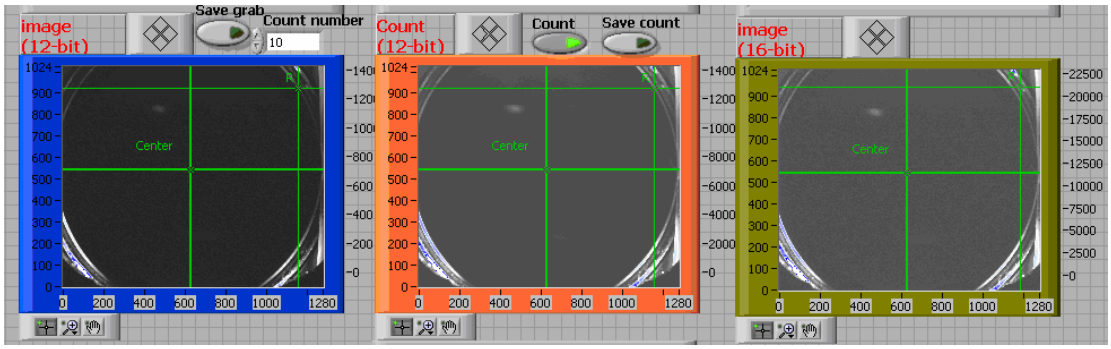

FIG.30. *Imaging VI*, front panel 2 to display images.

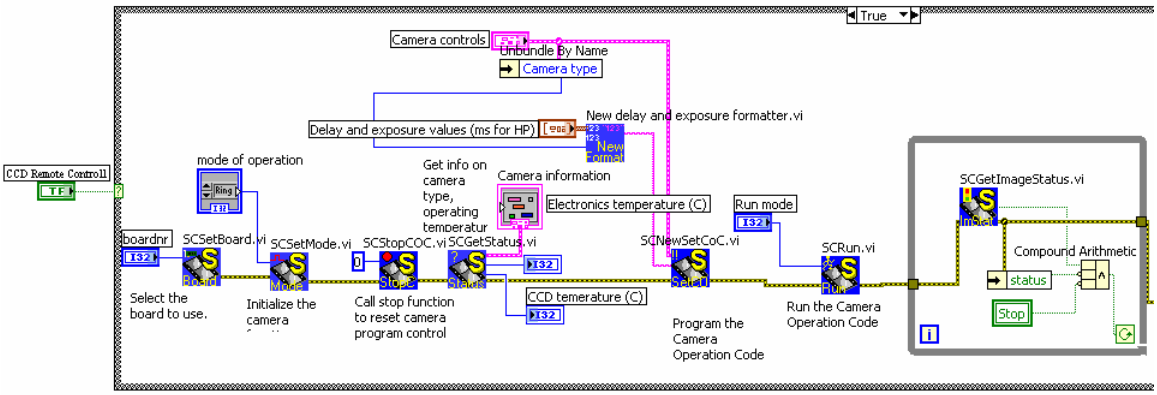

FIG.31. *Imaging VI*, block diagram.

4.6 Conclusion

The synchronization of the elements in the apparatus is important in the experimental procedure. This has been achieved by the virtual instruments created using LabVIEW 8.6.The programs written allow the user to set the experimental parameters, and collect data using the data acquisition system. Since the programs support modularity, it is also possible to add other components to the same programs in the future without disrupting the existing modules.

References for Chapter 4

[1]S. Sumathi and P. Surekha, LabVIEW based advanced instrumentation systems, Springer (2007).

[2] http://www.ni.com

[3]LabVIEW help menu

[4]Stanford Research Systems, Series PS 300, User Manual (1998).

[5]Stanford Research Systems, DG 525, User Manual (1999).

[6]National Instruments, DAQ 6023E/6024E/6025E, User Manual, January (1999).

[7]MSO3000 and DPO3000 Series Digital Phosphor Oscilloscopes User Manual, Tektronix

[8]D. M. Bolodovsky, Photodissociation dynamics of bromine chloride probed by velocity map imaging, M. Sc. thesis, Queen's University (2006).

[9]C. Romanescu, Velocity imaging of the photodissociation and photoionization dynamics of hydrogen chloride and hydrogen bromide, Ph. D. thesis, Queen's University (2007).

[10]C. Elliott, V. Vijayakumar, W. Zink, and R. Hansen, National Instrument LabVIEW: A programming environment for laboratory automation and measurement, The association for Laboratory Automation, (2007).

[11]SensiCam Optikon, Operating Instructions (1999).

[12]LabVIEW drivers for Sensicam Version 3.0.

Chapter 5
Photolysis of Amorphous Solid Methanol at 157 nm

5.0 Background

During the period from November 2008 – December 2008 I had the opportunity to work with Prof. Masahiro Kawasaki's research group in Kyoto University, Japan under an Ontario Centre for Excellence fellowship. During this period I became involved in experiments on the photochemistry of methanol ice as part of the preliminary experiments required for the development of the VMI apparatus at Queen's University. Upon my return I was able to perform simulations of the photofragments using PGOPHER software (by C. M. Western, University of Bristol) with the help of postdoctoral fellow, Wei Guo. This chapter is based on the experiments performed in Kyoto. The figures used in the experimental and results sections in this chapter have been reproduced from a publication co-authored by my collaborators and myself.

5.1 Introduction

Interstellar dust grains, with ice mantles coating their surface are rich with numerous chemical compounds such as H_2O, NH_3, CH_4, O_2, N_2, CO, CO_2 and H_2CO. As interstellar dust grains are continuously exposed to a low flux of UV photons, molecular bonds are broken within femtoseconds and the photofragments recombine, giving rise to complex

molecules. The production pathways of such molecules have been of great astrophysical interest.[1–4]

Methanol is also known to be a primordial constituent found abundantly on the icy mantle of dust grains, comets and other solar bodies.[2] Mumma *et al.*[5] reported that the abundance of methanol in Oort cloud comets is 1 – 3% relative to water. The photochemistry of the methanol–rich interstellar medium is expected to form large organic molecules.

Various dissociation mechanisms at 157 nm for methanol in the gas phase have been reported.[6,7] Lee *et al.*[8] suggested that the detected photoproducts were formed through the channels given in reactions (3.1–3.5) and that secondary dissociation occurs from CH_3O and H_2CO.

$$CH_3OH + h\upsilon \rightarrow CH_3O + H \quad (3.1)$$

$$CH_3OH + h\upsilon \rightarrow H_2CO + 2H \quad (3.2)$$

$$CH_3OH + h\upsilon \rightarrow H_2CO + H_2 \quad (3.3)$$

$$CH_3OH + h\upsilon \rightarrow CO + 2H_2 \quad (3.4)$$

$$CH_3OH + h\upsilon \rightarrow CH_3 + OH \quad (3.5)$$

Satyapal *et al.*[9] investigated the possible bond cleavage in gas phase methanol at 157 nm and reported that the O–H cleavage channel through reaction (3.1) was dominant with a quantum yield of (0.86 ± 0.1). The remainder was thought to be through the C–O cleavage channel via reaction (3.5). However, this contribution had not been quantified.[1] The photodissociation of solid methanol is more complex than in the gaseous phase since the photofragments are trapped in the site of production. Hence, the photochemistry of solid methanol has received much attention during the recent years.

Gerakines *et al.*[2] have studied the UV photochemistry of pure methanol ice samples at 10 K through infrared absorption spectroscopy. They reported the formation of carbon monoxide (CO), methyl formate (H_3COHCO), carbon dioxide (CO_2), methane (CH_4), formyl radical (HCO), formaldehyde (H_2CO), and hydrogen (H_2), as given in Figure 32, which was indicative of a complex photochemistry for methanol.[1,2] However, they could not detect the primary CH_3 and OH fragments. The possible reaction pathways for the products obtained from photodissociated solid methanol are given in reactions (3.6 – 3.14).[1,2,4] The primary photo products from the photodissociation of solid methanol may further react with the solid methanol matrix to produce secondary photoproducts.

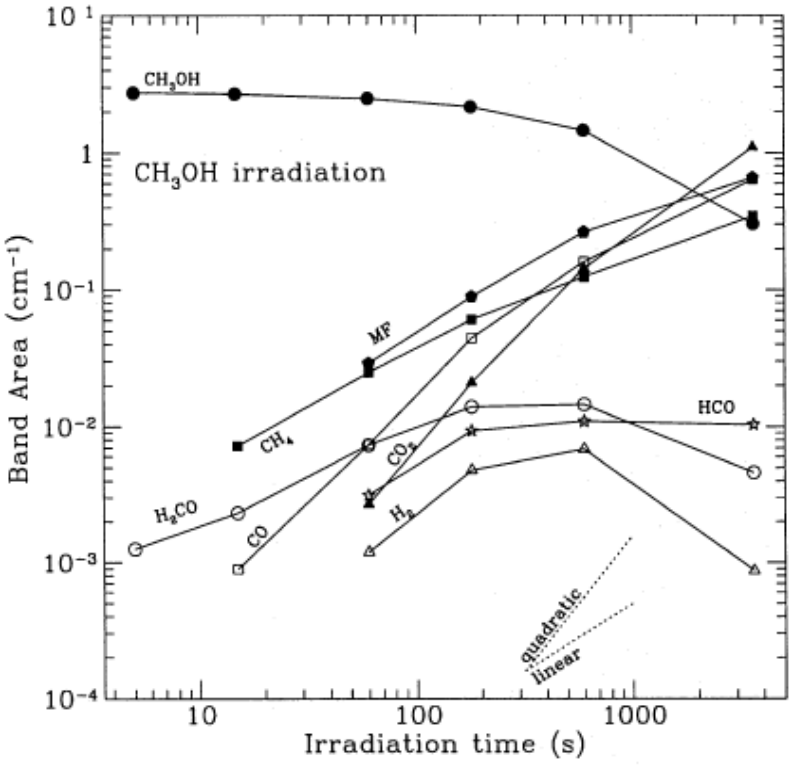

FIG.32. Evolution of features in CH_3OH irradiation. MF= methyl formate.

Reproduced from Gerakines *et al.*[2]

Hama *et al.*[10] have reported the mechanisms for hydrogen atom abstraction, recombination and hydrogen molecule elimination from solid methanol photodissociation at 90 K (reactions 3.6 – 3.9), using REMPI technique.

$$CH_3OH + h\upsilon \rightarrow \quad H_2CO + H_2 \tag{3.6}$$

$$CH_3OH + h\upsilon \rightarrow \quad CH_2OH + H \tag{3.7}$$

$$CH_3OH + h\upsilon \rightarrow \quad CH_2O + H_2 \tag{3.8}$$

$$CH_3OH + H \rightarrow \ CH_2OH + H_2 \quad (3.9)$$

$$H_2CO + h\upsilon \rightarrow \ CO + H_2 \quad (3.10)$$

$$H_2CO + HCOH \rightarrow \ CH_3OH + CO \quad (3.11)$$

$$H_2CO + h\upsilon \rightarrow \ CO + H_2 \quad (3.12)$$

$$H_2CO + H_2CO \rightarrow H_3COHCO \quad (3.13)$$

$$CH_3OH + h\upsilon \rightarrow \ CH_4 + O(^1D) \quad (3.14)$$

However, reaction (3.14) is not observed in the gas phase. Gerakines *et al.* reported that further investigation was required to determine if methane was a primary photo product of photodissociated solid methanol.[1,2]

This chapter reports the mechanisms for production and the possible reactions of CH_3 and OH from the 157 nm photodissociation of Amorphous Solid Methanol (ASM) at 90 K, using REMPI to determine their translational and internal energy distributions. Possible second order reactions on ASM are also discussed. An attempt was also made to detect $O(^1D)$ and $O(^3P)$.

5.2 Experimental

The photodissociation of solid methanol was performed in a high vacuum chamber, equipped with two turbo molecular pumps operating in tandem (Shimadzu 800 and 50 Ls^{-1}), a pulsed molecular beam, an excimer laser and two dye lasers.[11-13] The base pressure of the vacuum chamber was maintained at 5×10^{-7} Torr, using the two turbo molecular pumps. An optically flat sapphire substrate, sputter–coated with a thin polycrystalline film of Au (111), was mounted in the center of the chamber by a liquid nitrogen–cooled manipulator. The substrate temperature was controlled by heating a tantalum filament, attached to the substrate.

ASM films were prepared by backfilling the deposition of methanol vapor on to the gold substrate at 90 K for 60 min with an exposure of 1500 L (1 L = 1×10^{-7} Torr). UV photoirradiation and multiphoton ionization detection of CH_3 and OH were performed at a substrate temperature of 90 K. A 157 nm laser (Lambda Physik, OPTexPro) with a pulse duration of 10 ns was incident on the ASM surface at an angle of 80º to the surface at a fluence, F < 0.1 mJ $cm^{-2}pulse^{-1}$. CH_3 products were ionized at a distance of 2 mm from the substrate surface by (2+1) REMPI through the $4p_z\,{}^2A_2''\left(v'=0\right)\leftarrow X\,{}^2A_2''\left(v''=0\right)$ transition at 285–287 nm, and collected with a small mass spectrometer aligned perpendicular to the ice surface.[14]

OH products were ionized 4 mm above the substrate surface by (2+1) REMPI via the $D^2\Sigma^-(v'=0) \leftarrow X^2\Pi(v''=0)$ transition at 243.5–244.5 nm and also the $D^2\Sigma^-(v'=1) \leftarrow X^2\Pi(v''=0)$ and $3^2\Sigma^-(v'=0) \leftarrow X^2\Pi(v''=1)$ transitions at 237.5–237.7 nm.[15] The rotational structure of the of the measured spectra was simulated using the PGOPHER software package[16], and thus the rotational temperatures of the products were determined. Figure 33 illustrates the experimental set up.

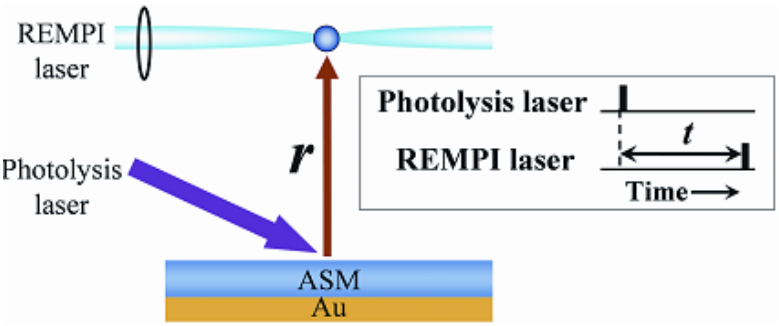

FIG.33. Schematic illustration of the experiment.
Photofragments from the 157 nm photodissociation of ASM are detected by the REMPI technique. The timing plot for measurements of a TOF spectrum is shown in the inset where the delay time *t* between photolysis and probe laser pulses corresponds to the TOF. *r* is the vertical distance between the disk substrate and the REMPI detection point. The VUV photoirradiated area is a disk with a radius of 6 mm.

Reproducd from Hama *et al.*[1]

Detection of $O(^1D_2), O(^3P_{J=2,1,0})$ atoms by (2+1) REMPI via the $O(^1F_3 \leftarrow ^1D_2)$ transition at 203.8 nm, $O(^3P_J - ^3P_J)$ transition at 225.6 – 226.4 nm was unsuccessful as no signal was observed.[18–20] Yabushita *et al.*[20] and Hama *et al.*[21, 22] have previously detected $O(^1D_2), O(^3P_{J=2,1,0})$ atoms by the same REMPI setup from the 157 nm photolysis of amorphous solid water at 90 K.[1]

The possibility of the measured photoproduct distributions being influenced by the photoproducts that are accumulated on the surface after prolonged irradiation was eliminated by continually refreshing the ASM surface by intermissive exposure to CH_3OH vapor. This was achieved by opening the pulsed valve to deposit a fresh layer of ASM after each laser shot.

For the CH_3OH/H_2O co–deposited ice photolysis experiments, CH_3OH/H_2O (1:1) mixed vapor was deposited on the gold substrate. The exposure of the CH_3OH/H_2O mixture was typically 1500 L. The TOF spectra of the CH_3 and OH photo fragments were taken as a function of time delay *t*, between photolysis and probe laser pulses. The time delay was controlled by a delay generator (Stanford Research) to allow the observation of the flight time of products.

The measured TOF spectra, $S(a_i,t, T_{trans})$, was fitted to a sum of Maxwell–Boltzmann (MB) distributions, S_{MB}, each defined by their respective translational temperature, T_{trans}. The coefficient, a_i, was used to define the relative population of each MB distribution.

$$S(a_i, t, T_{trans}) = \Sigma\ a_i S_{MB}(t, T_{trans}), \quad (3.15)$$

$$S_{MB}(t, T_{trans}) = r^3 t^{-4} \exp[-mr^2 / (2k_B T_{trans} t^2)] \quad (3.16)$$

where r is the flight distance of the photofragment. The MB distribution, $P_{MB}(E_t)$, as a function of translational energy, E_t, is characterized by the averaged translational energy, $\langle E_t \rangle = 2k_B T_{trans}$ where k_B is the Boltzmann constant.[23, 24]

$$P_{MB}(E_t) = (k_B T_{trans})^{-2} E_t \exp[-E_t/(k_B T_{trans})], \quad (3.17)$$

The signals are assumed to come from a VUV photoirradiation area with a radius of 6 mm. As given in Figure 34, the flight length is defined by $\left(r^2 + R^2\right)^{1/2}$, and the detection probability is proportional to $2\pi R \partial R / \left(r^2 + R^2\right)$ where r=2 and 4 mm for CH_3 and OH respectively, and $0 \le R \le 6$ mm.[1,11] The variable R is the radius of the irradiation area. For the angular distribution of the photofragments from the ice surface $\cos^n \theta$, where θ is the polar coordinate, n = 0 was assumed in the best fitting procedures as the parent CH_3OH molecules adsorb randomly on the ASM surface.[1]

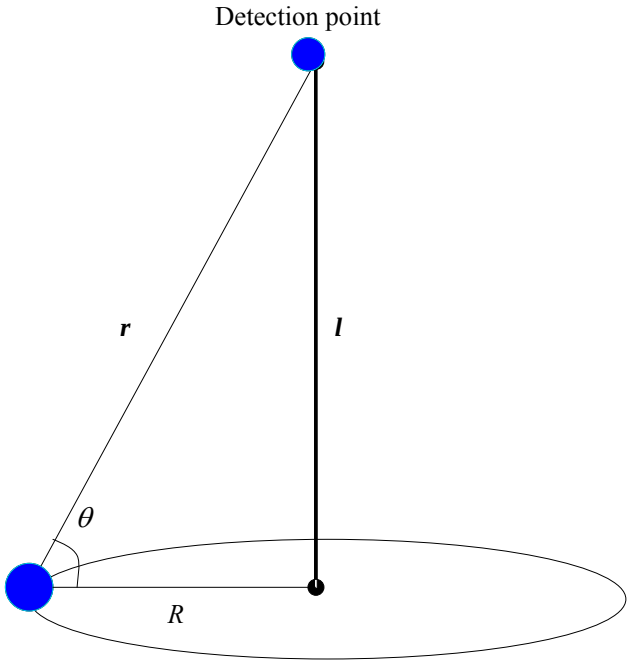

FIG.34. Detection of the photofragment from the surface. A circle indicates the irradiation area on the substrate. *l* is the distance between substrate and the detection point. *R* is the maximum radius of the irradiation area.

Reproduced from Yabushita *et al.*[20]

5.3 Simulation of (2+1) REMPI spectra

The (2+1) REMPI spectra for the $4p_z\,{}^2A_2''(v'=0) \leftarrow X\,{}^2A_2''(v''=0)$ transition of CH_3 products following was simulated by the Pgopher software package[16], by using the spectral parameters reported by Black and Powis.[14] The $4p_z\,{}^2A_2''(v'=0)$ state

predissociates with a level dependent efficiency and this phenomenon affects REMPI line intensities and line width.[14] The two photon transition probability is carried by two components ranked zero and two. The zero component contributes only to the intense central Q branch, while the component ranked two contributes to *O, P, Q, R* and *S* branches.

Similarly the simulation for OH products was performed using the spectral parameters available in current literature.[15,17] The two photon absorption cross section reported by Greenslade *et al.*[15] allows the estimation of the OH (v=1) / OH (v=0) population ratio.[1]

5.4 Results

5.4.1 Kinetic energy and rotational energy distribution of CH_3

Figure 35 (a) shows the REMPI rotational spectrum of CH_3 (v''=0) products following the 157 nm photolysis of freshly deposited ASM recorded at a fixed delay of t = 6.0 μs . The spectrum is assigned to the to $4p_z\,{}^2A_2''(v'=0) \leftarrow X\,{}^2A_2''(v''=0)$ transition.[14,26] The spectral simulation shown in figure 35 (b) determines the rotational temperature T_{rot} to be 150 ± 50 K ($\langle E_{rot} \rangle = 1.2 \pm 0.4$ kJ mol^{-1}). Figure 36 shows the congested Q branch in the TOF spectrum of CH_3 monitored at a REMPI wavelength of 286.0 nm.[1] This

spectrum was reproduced by the sum of two MB distributions with $T_{trans} = 3000 \pm 1000$ K ($<E_{trans}> = 49.9 \pm 16.6$ kJ mol^{-1}) and $T_{trans} = 90 \pm 20$ K ($<E_{trans}> = 1.5 \pm 0.3$ kJ mol^{-1}) as shown in Table 3. The signal intensity of the T_{trans} = 3000 K component was weak. Hence, the rotationally resolved REMPI spectrum has been difficult to characterize in terms of T_{rot}.

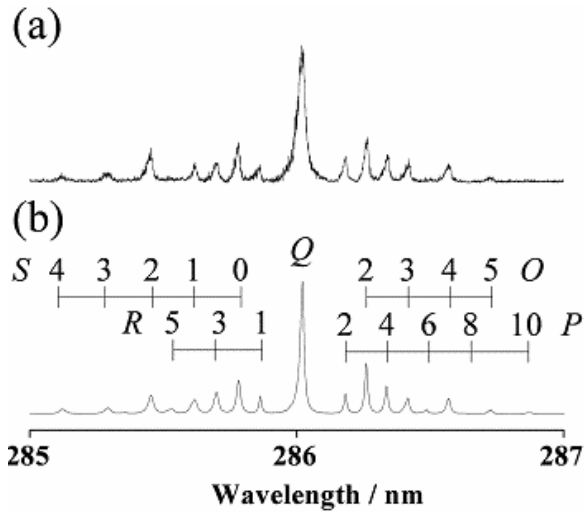

FIG.35. (a) (2+1) REMPI excitation spectrum of CH_3 radicals from the 157 nm photolysis of a fresh ASM sample at 90 K, recorded at t = 6.0 μs. (b) Simulated REMPI excitation spectrum of CH_3 radicals, resonance enhanced at the two photon energy by the $4p_z\,^2A_2''(v' = 0)$ level, assuming a Boltzmann distribution rotational state population distribution with T_{rot} = 150 K.

TABLE 3. Translational and rotational temperatures and energies of CH_3 ($v = 0$) products.

Time-of-flight component, contributions	Translational energy E_T (kJ mol^{-1})	Rotational temperature T_{rot} (K)	Translational energy E_R
CH_3 (T_{trans} = 3000 K, 10%)	49.9 ± 2.0	[a]	[a]
CH_3 (T_{trans} = 90 K, 90%)	1.5 ± 0.3	150 ± 50[b]	1.2 ± 0.4[b]

[a]The rotational spectrum could not be characterized by a specific T_{rot} because of the weakness of the signal intensity

[b]From spectra recorded at t=6.0 μs .

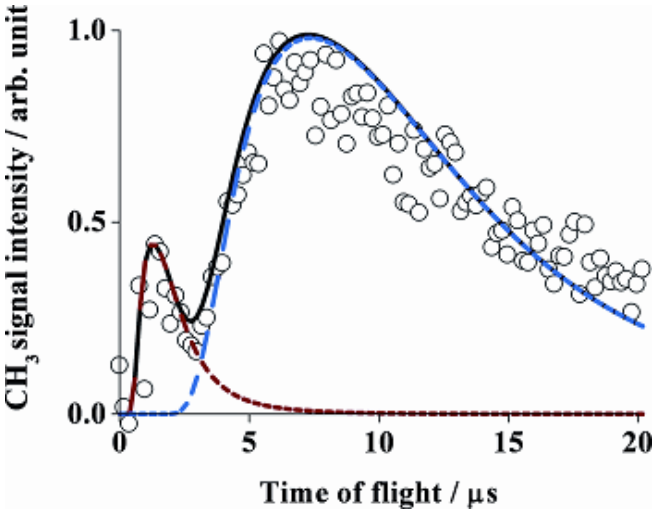

FIG.36. TOF spectrum of CH_3 radicals from the 157nm photolysis of a fresh ASM sample, monitoring on the Q branch of the (2+1) REMPI spectrum shown in Fig. 35. The solid curves are fits to the data derived assuming two MB distributions with T_{trans} = 3000 K (10 %) and 90 K (90 %). The vertical flight distance used in these experiments is 2 mm.

5.4.2 Kinetic energy and rotational distribution of the OH radical

Figure 37 (a) shows the REMPI rotational spectrum of OH (v=0) products following the 157 nm photolysis of freshly deposited ASM recorded at a fixed delay of t = 2.0 μs. The spectral simulation shown in figure 37 (b) determines the rotational temperature T_{rot} (v=0) to be 300 ± 100 K ($\langle E_{rot} \rangle = 2.5 \pm 0.8$ kJ mol^{-1}). Figures 38 (a) and 38 (b) show TOF spectra for OH (v=0) and OH (v=1) obtained by monitoring the $R_1(1)$ + $R_1(5)$ line and $R_1(2)$ line respectively, in the REMPI spectrum.[1] Both spectra were reproduced by a single MB distribution with $T_{trans} = 3000 \pm 500$ K ($\langle E_{trans} \rangle = 49.9 \pm 16.6$ kJ mol^{-1}). In contrast to CH_3 products the T_{trans} = 90 K component was not detected. The OH REMPI spectrum in figure 39 (a) shows the overlapping contributions from OH (v=0) and OH (v=1) recorded at t = 2.0 μs. The spectral simulation shown in figure 38 (b) determines the rotational temperature T_{rot}(v=0) to be 300 ± 100 K ($\langle E_{rot} \rangle = 2.5 \pm 0.8$ kJ mol^{-1}) and T_{rot}(v=1) to be 200 ± 50 K ($\langle E_{rot} \rangle = 1.7 \pm 0.4$ kJ mol^{-1}) as summarized in Table 4. The OH (v=1) / OH (v=0) population ratio is 0.2 ± 0.1.

TABLE 4. Translational and rotational temperatures and energies of OH (v = 0 and 1) products.

	OH(v = 0)		OH(v=1)[a]	
	Translation	Rotation	Translation	Rotation
Temperature (K)	3000 ± 500	300 ± 100[b]	3000 ± 500	200 ± 50[b]
Energy (kcal/mol)	49.9 ± 8.3	2.5 ± 0.8	49.9 ± 8.3	1.7 ± 0.4

[a] Population ratio OH (v=1) / OH (v=0) = 0.2 ± 0.1

[b] time-of-flight = 2.0 μs .

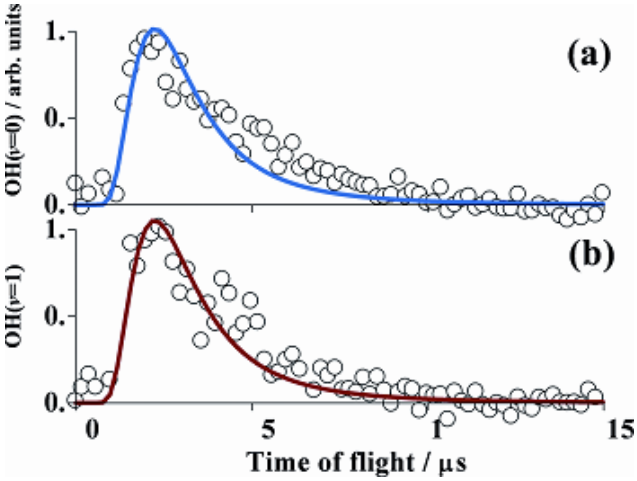

FIG.38. TOF spectra of OH radicals from the 157 nm photolysis of a fresh ASM sample, obtained by monitoring (a) the R_1 (1) + R_1 (5) line in the OH $D^2\Sigma^-\left(v'=0\right)\leftarrow X^2\Pi\left(v''=0\right)$ two–photon transition and (b) the R_1 (2) line in the OH $3^2\Sigma^-\left(v'=0\right)\leftarrow X^2\Pi\left(v''=1\right)$ two–photon transition. The solid curves are fits to the data derived assuming a MB translational energy distribution with T_{trans} = 3000 K in both cases. The vertical flight distance used in these experiments is 4 mm.

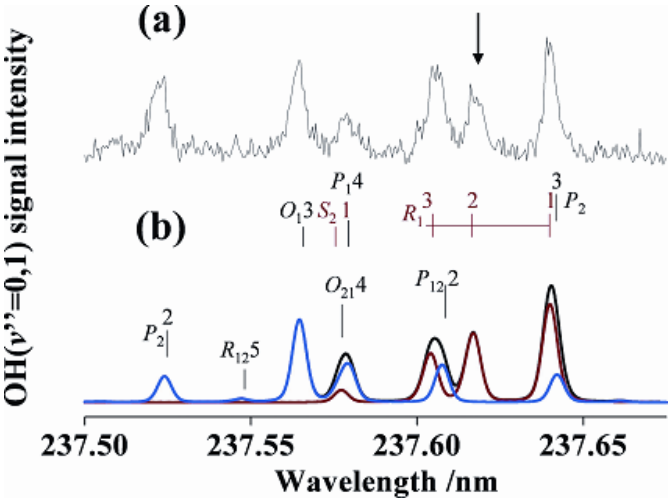

FIG.39. (a) (2+1) REMPI excitation spectrum of OH radicals from the 157 nm photolysis of a fresh ASM sample at 90 K recorded at t = 2.0 μs. (b) Simulation of relevant parts of the overlapping $D^2\Sigma^-\left(v'=1\right)\leftarrow X^2\Pi\left(v''=0\right)$ and $3^2\Sigma^-\left(v'=0\right)\leftarrow X^2\Pi\left(v''=1\right)$ two-photon transitions of OH assuming Boltzmann rotational state population distribution with T_{rot} (v'' = 0) = 300 K (blue line) and T_{rot} (v'' = 1) = 200 K (red line). The black line is the sum of the spectral simulations. The arrow indicates the R_1 (2) line used when measuring the TOF spectrum.

5.4.3 Additional 157 nm photolysis experiments on ASM

The effect of the secondary photoprocesses on the ASM surface and in the bulk, on the desorbing CH_3 and OH were assessed by measuring the TOF spectra of these species after 30 min of photoirradiation without intermissive injection of CH_3OH vapor into the chamber. No disparities in TOF or REMPI spectra were observed between the CH_3 or OH products for fresh or photoirradiated ASM samples. This implies that the desorbed CH_3 and OH species are formed through the C–O cleavage channel and that the secondary photoprocesses on the ASM surface and in the bulk make no contribution to their formation.

REMPI signals for $O(^1D)$ and $O(^3P)$ atoms were not observed in the TOF range at 0.5 μs $\leq t \leq$ 30 μs.[1] Hama *et al.* have previously detected $O(^1D)$ and $O(^3P)$ following the 157 nm photodissociation of H_2O and H_2O_2.[21,22] The lack of detectable $O(^1D)$ and $O(^3P)$ atoms from ASM is in agreement with methanol photolysis in the gas phase reported by Hariach *et al.*[7] and Lee *et al.*[8] They reported that formation of methane and $O(^1D)$ or $O(^3P)$ atoms through reactions (3.14) and (3.18) is insignificant in the photolysis of methanol.

$$CH_3OH + h\upsilon \rightarrow CH_4 + O(^1D) \quad (3.14)$$

$$CH_3OH + h\upsilon \rightarrow CH_4 + O(^3P) \quad (3.18)$$

In order to ensure that the CH_3 distribution was not effected by the background water vapor deposition, the TOF signal was measured from a photoirradiated 1:1 mixture of

CH_3OH/ H_2O ice. The TOF intensities for CH_3 in both components at T_{trans} = 3000 and 90 K decreased. Additionally, similar to the fresh ASM sample, a majority of the CH_3 fragments are accommodated to the substrate temperature of 90 K. The effects on the OH distribution could not be determined in a similar manner as the photolysis of H_2O contributes to the OH distribution.[32,33]

5.5 Discussion

The photodissociation of methanol in the condensed phase through the C–O bond cleavage channel is given in reaction (3.19) where ("ads") is the condensed or the adsorbed species and ('i') is the ASM vacuum interface.[1]

$$CH_3OH(ads) + h\nu \rightarrow CH_3(i) + OH(i) \quad \Delta H = 422.6 \text{ kJ mol}^{-1} \quad (3.19)$$

The photonic energy provided for the reaction at 157 nm is 757.3 kJ mol^{-1} and the energy available for this reaction has been calculated as 334.7 kJ mol^{-1}.[1,27,28]

In the gas phase photolysis of CH_3OH at 157 nm, Lee *et al*.[8] and Harich *et al*.[6,7] have shown that the distribution of the total kinetic energy for CH_3 and OH is 217.6 kJ mol^{-1}. The translational kinetic energy partitioned between CH_3 and OH, according to the conservation of momentum, is calculated respectively as 117.2 and 100.4 kJ mol^{-1}.

In the condensed phase, the average center of mass translational energy for the photodesorbed CH_3 and OH products is only 99.8 kJ mol^{-1}. This reduction in partitioning of E_{avail} (3.19) could be due to the dissipation of energy into the ASM bulk.

5.5.1 CH_3 radical formation from the photolysis of fresh ASM

The TOF spectrum of CH_3 products measured at 157 nm was attributed to the sum of two MB components. They are distinguished as a high–temperature, fast component at T_{trans} = 3000 K and a surface–accommodated, slow component at T_{trans} = 90 K, with respective contributions of 10% and 90%. A majority of the CH_3 fragments are accommodated to the substrate temperature of 90 K and, as given in Table I, the translational and rotational energies are considerably lower than E_{avail}(19). Hence, the dominance of the surface–accommodated component is accredited to nascent CH_3 products formed in the ASM bulk losing a substantial amount of energy, as a consequence of undergoing collisions within the porous ASM structure before they are detected at the surface. A fraction of the nascent CH_3 is produced directly at the ASM surface and desorbs without interacting with neighboring molecules while sustaining a high translational temperature of 3000 K. The formation of these two components of nascent CH_3 is given in reactions (3.20) and (3.21).

$$CH_3OH + h\nu \rightarrow CH_3\,(T_{trans} = 3000\ K) + OH \qquad (3.20)$$

$$CH_3\,(3000\ K) \xrightarrow{collision} CH_3\,(90\ K) \qquad (3.21)$$

In addition to this, CH_3 photoproducts that partake in secondary photoprocesses in the ASM bulk may remain undetected.[2] Jodkowski *et al.*[29] have reported the activation energies E_a, available for hydrogen abstraction reactions by CH_3 photoproducts in the gas phase (reactions 3.22, 3.23).[1]

	ΔH	E_a (kJ mol^{-1})	
$CH_3(i) + CH_3OH(ads) \rightarrow CH_4(i) + CH_2OH(i)$	4.2	58.6	(3.22)
$CH_3(i) + CH_3OH(ads) \rightarrow CH_4(i) + CH_3O(i)$	33.5	56.9	(3.23)

Hence, the high temperature component of nascent CH_3 with $\langle E_{trans} \rangle$ = 49.9 kJ mol^{-1} may participate in this secondary photoprocess. However, a major fraction of nascent CH_3 molecules is accommodated to the surface temperature, and their average energy (~ 2.7 kJ mol^{-1}) is insufficient to overcome the activation barrier of hydrogen abstraction. Consequently, the thermally equilibrated CH_3 will be detected as primary photodissociation product.

At high photon fluxes CH_3 may be further removed through the recombination reactions with H–atom photoproducts to produce methane.

$$CH_3(i) + H(i) + M \rightarrow CH_4(i) + M \qquad \Delta H = -439.3 \text{ kJ mol}^{-1} \qquad (3.24)$$

The H atoms formed on amorphous ice are known to move between 6 – 60 Å leading to an efficienct recombination process.[30] The formation of H atoms on ASM at 90 K following the 157 nm photodissociation through reactions (3.1) and (3.7) has been reported by Hama *et al.* [10] In studies on the ultraviolet processing of ASM at 10 K, Gerakines *et al.*[2] detected the IR absorption feature for CH_4, but the absorption feature for CH_3 was not detected. It can be inferred that this was a consequence of the CH_3 radicals being recombined with the mobile H atoms via reaction (3.24).

In the CH_3OH/H_2O experiment, the intensities of both 3000 and 90 K CH_3 components were reduced. This can be attributed to the reduction in the CH_3OH density on the surface or to the recombination of CH_3 radicals via reaction (3.24), or to the reaction of CH_3 radicals with OH radicals produced from the photolysis of H_2O. The possibility of the reaction between CH_3 radicals and solid water can be eliminated due to the large activation energy requirement in reaction (3.25). [31]

$$CH_3(i) + H_2O(ads) \rightarrow CH_4(i) + OH(i) \qquad (3.25)$$

$$\Delta H = 104.6 \text{ kJ mol}^{-1} \quad E_a = 138.1 \text{kJ mol}^{-1}$$

The ratio of the 3000 and 90 K components in the TOF profile of CH_3 products from the mixed ice of CH_3OH/ H_2O was found to be similar to that from the fresh ASM samples, with a dominant fraction of the CH_3 radicals being accommodated to the substrate

temperature (90 K). This implies that the CH_3 products desorbed without reaction with solid water.[1]

5.5.2 OH radical formation from the photolysis of fresh ASM

The translational energies of OH (v = 0 and 1) from fresh ASM are characterized by the temperature T_{trans} = 3000 ± 500 K ($\langle E_{trans} \rangle$ = 49.9 ± 8.3 kJ mol^{-1}). The OH rotational temperatures, $T_{rot}(v=0)$ = 300 ± 100 K and $T_{rot}(v=1)$ = 200 ± 50 K, are not accommodated to the substrate temperature of 90 K.[1] This implies that the nascent OH photofragments originate from the ASM surface. The lack of a thermally equilibrated OH component also suggests that OH formed in the bulk may be trapped or reacts with molecules in the bulk as given in reactions (3.20) and (3.26).[1,32,33] Andersson *et al.* reported that the desorption probability of OH was less than 3% per monolayer in the top 3 monolayers of water ice at 10 K.[34,35]

$$CH_3OH + h\nu\,(157\text{ nm}) \rightarrow CH_3 + OH(T_{trans}=3000\text{ K}) \quad (3.20)$$

$$OH\ (3000\text{ K}) \xrightarrow{collision} \text{trapped or reacted with ASM} \quad (3.26)$$

The OH radicals originating in the bulk may progress to a maximum distance of 5 Å at 10 K in bulk water ice and more than 60 Å in the top 3 monolayers.[32,33] The presumable hydrogen abstraction reactions are given in reactions (3.27) and (3.28).[36] The activation energies for the same reactions in the gas phase have been reported by Jodkowski *et al.* [29]

	ΔH	E_a(kJ mol^{-1})	
$OH(i) + CH_3OH(ads) \rightarrow H_2O(i) + CH_2OH(i)$	-50.2	3.8	(3.27)
$OH(i) + CH_3OH(ads) \rightarrow H_2O(i) + CH_3O(i)$	-25.1	14.6	(3.28)

Considering the translational energies for nascent OH given in Table II, it can be inferred that the activation barrier for the hydrogen abstraction reactions from ASM is easily overcome.

5.5.3 Other possible secondary photoprocesses

Jasper *et al.*[37] have reported the formation of a variety of reactive radicals and molecules, such as CH_3OH, $CH_2 + H_2O$, $HCOH + H_2$, $H_2CO + H_2$, $CH_3O + H$ and $CH_2OH + H$, through the bimolecular reaction of CH_3 and OH radicals in the gas phase. In a study on the ultraviolet photolysis of methane–water ice mixtures at 20 K, Hodyss *et al.*[38] reported that OH radicals produced from the photodissociation of water react with methane to form CH_3 radicals, which in turn recombine with OH to form methanol, as given in reaction (3.29).

$$CH_3(i) + OH(i) + M \rightarrow CH_3OH(ads) + M \qquad (3.29)$$

$$\Delta H = -422.6 \text{ kJ mol}^{-1}$$

In addition to these reactions Hodyss *et al.*[38] detected the formation of ethane through the recombination of CH_3 radicals via reaction (3.30) where CH_3 resided in adjacent sites in the solid water matrix.

$$CH_3(i) + CH_3(i) + M \rightarrow C_2H_6(i) + M \qquad (3.30)$$

$$\Delta H = -376.6 \text{ kJ mol}^{-1}$$

Since ethane was not detected by Gerakines *et al.*[2] in the ultraviolet processing of solid CH_3OH at 10 K, it can be inferred that reaction (3.30) would only arise, if nascent CH_3 is less likely to encounter other reactive species, such as H, OH or CH_3OH.

5.6 Conclusion

The formation of photofragments CH_3 (v=0) and OH (v=0 and 1) from the C–O bond cleavage channel has been investigated through the 157 nm irradiation of amorphous solid methanol at 90K. The low internal energies of the CH_3 photofragments suggest that the majority of the CH_3 photofragments are accommodated to the substrate temperature, and diffuse to the vacuum interface through the ASM bulk phase. However, the detected OH photofragments originated entirely from the ASM surface, and any OH formed in the bulk phase of amorphous solid methanol is trapped or reacts with molecules in the bulk. The TOF spectra of CH_3 photofragments from CH_3OH –H_2O ice sample suggest that the reactivity of solid water with CH_3 products is small.

As discussed in the literature review on chapter 2, similar reactions take place in amorphous solid water when dissociated species react to react further with water molecules.[39] Incident UV photons ($\lambda \leq 0.28 \mu m$) can cause the primary dissociation of water ice, yielding H + OH.[40,41] The photodissociation of trapped OH can produce O + H.[2] H atoms may further react with the water ice molecules to produce H_2 molecules through H abstraction, or the H atoms may recombine to produce H_2 (reactions 3.6 and 3.7).[30] This process is relevant to the formation of H_2 by the photolysis of water ice on dust grains in the warmer regions of the interstellar medium.[30]

$$HAB : H + HOH \rightarrow H_2 + OH \quad (3.6)$$

$$HR : H + H \rightarrow H_2 \quad (3.7)$$

More over, the OH photoproducts formed by the 157 nm photodissociation of ASW at 90 K, can recombine to produce H_2O_2 or may produce HO_2 as given in reactions (3.9) and (3.10).[2]

$$OH + OH \rightarrow H_2O_2 \quad (3.9)$$

$$OH + H_2O_2 \rightarrow H_2O + HO_2 \quad (3.10)$$

A majority of the studies on the photolysis of ASW, and its constituents have been directed towards investigating the products and the yields of reactions. The photolysis in the condensed phase is more complicated than in the gas phase, as a result of the secondary photo processes that take place in the ice matrix. Therefore, it is important

investigate the possible reaction channels in the energetic process. An understanding of the kinetic energy and internal energy distribution of the photoproducts would be imperative to provide a complete understanding of the reaction mechanisms.

References for Chapter 5

[1] T. Hama, M. Yokohama, A. Yabushita, M. Kawasaki, P. Wickramasinghe, W. Guo, H. –P. Loock, M. N. R. Ashfold, and C. M. Western, J. Chem. Phys. **131,** 224512 (2009).

[2]P. A. Gerakines, W. A. Schutte, and P. Ehrenfreund, Astron. Astrophys. **312**, 289 (1996).

[3]G. A. Baratta, G. Let, and M. E. Palumbo, Astron. Astrophys. **384**, 343 (2002).

[4]C. J. Bennett, S.–H. Chen, B.–J. Sun, A. H. H. Chang, and R. I. Kaiser, Astron. Astrophys. **660**, 1588 (2007).

[5]M. J. Mumma, M. A. DiSanti, K. Magee–Sauer, B. P. Bonev, G. L. Villanueva, H. Kawakita, N. D. Russo, E. L. Gibb, G. A. Blake, J. E. Lyke, R. D. Campbell, J. Aycock, A. Conrad, and G. M. Hill, Science **310**, 270 (2005).

[6]S. Harich, J. J. Lin, Y. T. Lee and X. Yang, J. Chem. Phys. **111**, 5 (1999).

[7]S. Harich, J. J. Lin, Y. T. Lee and X. Yang, J. Chem. Phys. **103**, 10324 (1999).

[8]S. H. Lee, H. I. Lee, and Y. T. Lee, J. Chem. Phys. **121**, 11053 (2004).

[9]S. Satyapal, J. Park, R. Bersohn, and B. J. Katz, J. Chem. Phys. **91**, 6873 (1989).

[10]T. Hama, M. Yokoyama, A. Yabushita, and M. Kawasaki, J. Chem. Phys. **30**, 164505 (2009).

[11]A. Yabushita, Y. Inoue, T. Senga, M. Kawasaki, and S. Sato, J. Phys. Chem. B **106**, 3151 (2002).

[12]A. Yabushita, Y. Hashikawa, A. Ikeda, M. Kawasaki, and H. Tachikawa, J. Chem. Phys. **120**, 5463 (2004).

[13]S. M. Dounce, J. Mundy , and H. L. Dai, J. Chem. Phys. **126**, 191111 (2007).

[14]J. F. Black and I. Powis, J. Chem. Phys. **89**, 3986 (1988).

[15]M. E. Greenslade, M. I. Lester, D. C. Radenovic, A. J. A. van Roij, and D. H. Parker, J. Chem. Phys.**123**, 074309 (2005).

[16]C. M. Western, PGOPHER, a program for simulating rotational structure, University of Bristol, available at http://pgopher.chm.bris.ac.uk.

[17]K. P. Huber and G. Herzberg (data prepared by J. W. Gallagher and R. D. Johnson, III), "Constants of Diatomic Molecules," in NIST Chemistry WebBook, NIST Standard Reference Database Number 69, P. J. Linstrom and W. G. Mallard, National Institute of Standards and Technology, Gaithersburg, MD, 20899, see http://webbook.nist.gov/ (retrieved 2009).

[18]S. T. Pratt, P. M. Dehmer, and J. L. Dehmer, Phys. Rev. A **43**, 4702 (1991).

[19]Y. Matsumi, N. Shafer, K. Tonokura, M. Kawasaki, Y.– L. Huang, and R. J. Gordon, J. Chem. Phys. **95**, 7311 (1991).

[20]A. Yabushita, T. Hama, M. Yokoyama, M. Kawasaki, S. Andersson, R. N. Dixon, M. N. R. Ashfold, and N. Watanabe, Astrophys. J. **699**, L80 (2009).

[21]T. Hama, A. Yabushita, M. Yokoyama, M. Kawasaki, and N. Watanabe, J. Chem. Phys. **131**, 114510 (2009).

[22]T. Hama, A. Yabushita, M. Yokoyama, M. Kawasaki, and N. Watanabe, J. Chem. Phys. **131**, 114511 (2009).

[23]F. M. Zimmermann and W. Ho, J. Chem. Phys. **100**, 7700 (1994).

[24]F. M. Zimmermann and W. Ho, Surf. Sci. Rep. **22**, 127 (1995).

[25]A. Yabushita, Y. Inoue, T. Senga, M. Kawasaki, and S. Sato, J. Phys. Chem. A **108**, 438 (2004).

[26]P. Quintana, R. F. Delmdahl, D. H. Parker, B. Martinez–Haya, F. J. Aoiz, L. Banares, and E. Verdasco, Chem. Phys. Lett. **325**, 146 (2000).

[27]Y.–P. Kuo, H.–C. Lu, Y.–J. Wu, B.–M. Cheng, and J. F. Ogilvie, Chem. Phys. Lett. **447**, 168 (2007).

[28]B.–M. Cheng, C.–P. Liu, W.–J. Lo, and Y.–P. Lee, Nucl. Instrum. Methods Phys. Res. A **467**, 1461 (2001).

[29]J. T. Jodkowski, M.–T. Rayez, J.–C. Rayez, T. Bérces, and S. Dóbé, J. Phys. Chem. A **103**, 3750 (1999).

[30]A. Yabushita, T. Hama, D. Iida, N. Kawanka, M. Kawasaki, N.Watanabe, M. N. R. Ashfold and H. –P. Loock, J. Chem. Phys. **129**, 044501 (2008).

[31]G. Bravo–Pérez, J. R. Alvarez–Idaboy, A. G. Jiménez, and A. Cruz–Torres, J. Chem. Phys. **310**, 213 (2005).

[32]A. Yabushita, T. Hama, D. Iida, and M. Kawasaki, J. Chem. Phys. **129**, 014709 (2008).

[33]T. Hama, A. Yabushita, M. Yokoyama, M. Kawasaki, and S. Andersson, J. Chem. Phys. **131**, 054508 (2009).

[34]S. Andersson, A. Al–Halabi, G.–J. Kroes, and E. F. van Dishoeck, J. Chem. Phys. **124**, 064715 (2006).

[35]S. Andersson and E. F. van Dishoeck, Astron. Astrophys. **491**, 907 (2008).

[36]M. C. Akin, N. G. Petrik, and G. A. Kimmel, J. Chem. Phys. **130**, 104710 (2009).

[37]A. W. Jasper, S. J. Klippenstein, L. B. Harding, and B. Ruscic, J. Phys. Chem. A **111**, 3932 (2007).

[38]R. Hodyss, P. V. Johnson, J. V. Stern, J. D. Goguen, and I. Kanik, Icarus **200**, 338 (2009).

[39]S. C. Schwentner, R. M. Schriever, and M. Chegui, J. Chem. Phys. **95**, 6124 (1991).

[40]I. H. Piette, R. C. Rempel, and H. E. Weaver, J. Chem. Phys. **30**, 1623 (1959).

Chapter 6
Summary

6.0 Summary

In the interstellar medium and in the polar regions of earth, water ice is a medium for chemical reactions when exposed to ultraviolet radiation. Amorphous solid water not only has fascinating photochemistry leading to the formation of photoproducts such as H_2, OH, H_2O_2 but it also can change the photochemistry of adsorbed species.

In experimental studies it has been found that the photo initiated reaction mechanisms between water ice and adsorbed species are dependent on the morphology of water ice. The morphology of water ice may be changed by modifying deposition conditions such as the temperature of the substrate, the incidence angle and the flux. Therefore it is necessary to be very specific about the ice matrix created in experimental studies. The morphology of the water ice matrix can be characterized by FT-IR spectroscopy as described in section 2.2.

The experimental studies conducted in Kyoto University on the 157 nm photolysis of the methanol- ice matrix probed by 2+1 REMPI demonstrates that many secondary photo processes take place in the ice matrix. Using the apparatus under development at Queen's University a significant amount of information about the ice matrix and the primary and

secondary photoproducts from the ice surface can be extracted through the combination of the REMPI spectroscopy and FT-IR spectroscopy. These studies will be valuable in illustrating the structural changes that take place in the ice matrix and will allow the reaction mechanisms for the secondary photoprocesses to be explored comprehensively. The addition of VMI spectroscopy expands this investigation further by providing information about kinetic and internal energy distributions of the desorbed species, and the dynamics taking place during photodissociation.

The present work involves the design and development of the VMI apparatus together with the development of software components required for experimental studies. Resolution characteristics of the apparatus were studied with ion trajectories simulations using the Simion 7.0 software package. These computations investigate the dependence of the resolution of the image on the ion optics voltage. Additionally, a software program written using Microsoft Visual Basic 6.0 was employed to simulate the experimental pattern observed on the position sensitive detector from the photoproducts desorbed from the ice matrix. This simulation will aid in predicting the velocity profile of the photoproducts, and thereby will be valuable in proposing mechanisms for reactions in water ice and its constituents.

The synchronization of the instrumental components is a vital aspect of the experiment. Therefore, virtual instruments have been created using LabVIEW 8.6 to control the main elements of the experiment such as the Molecular Beam Valve, triggering of photolysis

and probe laser pulses, and high voltages power supplies. Additionally, software components were developed to record the TOF spectra of the ionized photoproducts, to record the REMPI spectra, and to acquire the image of the ion cloud.

Finally, the preliminary work for the development of the VMI apparatus conducted through the photolysis of methanol ice at 157 nm photolysis using a different apparatus at the Kyoto University have been described. This experiment provides an appreciation of the experimental parameters and exemplifies the capabilities of the state selective detection of photoproducts following the photolysis of the ice matrix. Following this preliminary study it will be possible to simulate the water ice matrices in polar regions of the earth containing contaminants such as nitrates and sulfates using the VMI apparatus.

Appendix

```
Private Sub cmdReadFile_Click()
Dim Ekin(500), a(500), beta2(500), beta4(500)
pi = 3.141592
sumofa = 0
Dim R2 As Double

ChDir ("c:\Data\Piyumie\Monte Carlo Image Creation\") '  Change this path to where ever you want you work environment to be
   Open "inputfile.txt" For Input As #1
      Input #1, NumberofIons
      Input #1, Field
      Input #1, length
      i = 0

      Do While Not EOF(1)
         Input #1, Ekin(i), a(i), beta2(i), beta4(i)
         sumofa = sumofa + a(i)
         i = i + 1
      Loop
   Close #1
   txtNumberofIons.Text = NumberofIons
'    Text1.Text = beta2
'    Text2.Text = beta4

      numberofchannels = i - 1
      s = NumberofIons / sumofa
      Q = 96800
```

```
        Counter = 0

End Sub

Private Function acos(y As Double)
            Dim v As Double
            v = (y * 2 - 1)
            acos = (Atn(-v / Sqr(-v * v + 1)) + 2 * Atn(1))
End Function

Private Sub Command1_Click()
Dim Ekin(500), a(500), beta2(500), beta4(500)
Dim IntImage(1050, 1050) As Integer
Dim image(1050, 1050) As Byte
Dim R2, R1, R3 As Double

pi = 3.141592
sumofa = 0
maxEkin = 0

res = Val(Text3.Text)

For i = 0 To res
   For j = 0 To res
      image(i, j) = 0
      IntImage(i, j) = 0
   Next j
Next i
ChDir ("c:\Data\Piyumie\Monte Carlo Image Creation\")
```

```
    Open "inputfile.txt" For Input As #1
        Input #1, dummy
        Input #1, Field
        Input #1, length

        NumberofIons = Val(txtNumberofIons.Text)
'       beta2 = Val(Text1.Text)
'       beta4 = Val(Text2.Text)
        i = 0

        Do While Not EOF(1)

            Input #1, Ekin(i), a(i), beta2(i), beta4(i)
            sumofa = sumofa + a(i)
            If Ekin(i) > maxEkin Then maxEkin = Ekin(i)
            i = i + 1
        Loop
    Close #1



    numberofchannels = i - 1
        s = NumberofIons / sumofa
        Q = 96800
        Counter = 0
        maxrho = Q * length * Field / maxEkin
        maxRad = 1.1 * (2 * length / Sqr(maxrho)) ' add 10% to the radius to create frame
around image

    Open "outputfile.txt" For Output As #2
```

```
    Print #2, NumberofIons, Field, length

    For i = 0 To numberofchannels
        rho = Q * length * Field / Ekin(i)
        For j = 0 To a(i) * s
            R1 = Rnd()
            R2 = Rnd()
            R3 = Rnd()
            If ((beta2(i) * 0.5 * (3 * (Cos(R1 * pi) ^ 2) - 1) + 1/ 4 *pi) / (1 - beta2(i) * (-0.25 -
Sgn(beta2(i)) * 0.75))) > R2 Then
                theta = acos((R1))
                Counter = Counter + 1
                phi = R3 * 2 * pi
                X = 2 * length * Cos(phi) * Sin(theta) / Sqr(rho)
                Z = 2 * length * Cos(theta) / Sqr(rho)
                Print #2, X, Z
                XI = Int((Z / maxRad + 1) * res / 2): YI = Int((X / maxRad + 1) * res / 2):
IntImage(XI, YI) = IntImage(XI, YI) + 1
                If IntImage(XI, YI) > fullscale Then fullscale = IntImage(XI, YI)
            End If
        Next j
        ProgressBar1.Value = i / numberofchannels * 100

    Next i

    Close #2

    Label1.Caption = "Done:  " + Str$(Counter) + " ions"
```

```
If Check1.Value = False Then fullscale = 255

Open "Monte Carlo Image.raw" For Output As #4
   For i = 0 To res - 1
   For j = 0 To res - 2
      image(i, j) = Int(IntImage(i, j) * 255# / fullscale)
      Write #4, image(i, j),
   Next j
   Write #4, image(i, j + 1)
   Next i
Close #4

End Sub

Private Sub Command2_Click()
   End
End Sub

Private Sub Command3_Click()
   Call modBMP.pCreateBMPImage("BMP_Palette_bw.bny", "Monte Carlo Image.raw",
"Monte Carlo Image.bmp")

   Load frmBMP_Info
   frmBMP_Info.Show
End Sub
```